

## Aspects of boundary-value problem solutions with three-dimensional dislocation dynamics

D Weygand<sup>1</sup>, L H Friedman<sup>1</sup>, E Van der Giessen<sup>1</sup> and A Needleman<sup>2</sup>

<sup>1</sup> Netherlands Institute for Metals Research, University of Groningen, Department of Applied Physics, Micromechanics of Materials Group, Nijenborgh 4, 9747 AG Groningen, The Netherlands

<sup>2</sup> Brown University, Division of Engineering, Box D, Providence, RI 02912, USA

Received 11 December 2001, in final form 25 February 2002

Published 20 June 2002

Online at [stacks.iop.org/MSMSE/10/437](http://stacks.iop.org/MSMSE/10/437)

### Abstract

A three-dimensional discrete dislocation dynamics plasticity model is presented. The approach allows realistic boundary conditions on the specimen, as both stress and displacement fields of the dislocations are incorporated in the formulation. Emphasis is placed on various technical details in the formulation as well as on the implementation. The current implementation includes features necessary to model conservative motion of dislocations in presence of surfaces. These include details of the discretization of the evolving dislocation structure, the handling of junction formation and destruction, cross-slip and boundary conditions. Special attention is given to the treatment of dislocations that partly glide out of the material, including the treatment of image forces via the finite-element method.

### 1. Introduction

A conventional continuum-mechanics approach to the analysis of deformation in solids is appropriate when the wavelength of the deformation field is long compared to the lengthscale associated with the heterogeneity of the microstructure. For plastic flow in crystalline solids, this implies that the size of the specimen and the characteristic wavelength associated with the loading has to be much larger than the size-scale of the dislocation microstructure, in order that the latter can be averaged out to a continuum.

At sufficiently small scales, as in nano-indentation, or when one is interested in the local state at lengthscales comparable to the dislocation structure (see e.g. [1]), a description is needed where dislocations are treated as discrete entities. In large part because of the increased available computing power, discrete dislocation plasticity has gained much interest in the last decade. In this description of plastic deformation, the dislocations are treated individually, while the elastic medium in which they move is still treated as a continuum. The long-range elastic interactions between dislocations are naturally included in the elastic fields, while

short-range, i.e. atomistic, properties are to be supplemented through constitutive rules for dislocation motion, annihilation, cross-slip, etc.

There appear to be two key issues in the numerical implementation of discrete dislocation plasticity in three dimensions. The first issue is the description of the individual dislocations. Most methods currently in use, involve discretization of each dislocation. These schemes vary from a screw–edge representation (e.g. [2–4]), a representation with straight mixed segments (e.g. [5–7]) to one with a spline representation [8].

The second issue is the treatment of boundary-value problems. Apart from dedicated approaches to specific problems such as traction-free boundaries (e.g. [10]), currently there are a few general approaches in use. The first general approach is due to Van der Giessen and Needleman [11], which involves a decomposition into an analytical singular solution for infinite space and a correction for finite sample sizes by means of the finite-element method. This approach has been used subsequently by other authors (e.g. [4]). Somewhat related yet distinctly different approaches (e.g. [12, 13]) have been proposed in which finite-element methods are used in a different way.

Now that some basic experience has been obtained with these various techniques, it seems timely to critically assess the accuracy of the methods. The purpose of the present paper is to carefully explore various technical issues as they apply to a particular approach, namely, one based on the mixed-character straight segment discretization of Kukta [6] and using the Van der Giessen–Needleman [11] decomposition to solve boundary-value problems.

The remainder of the paper is organized as follows. For the purpose of demonstrating quantitative accuracy, a summary of the entire approach is given with due attention to technical details that govern the numerical accuracy of the solution. Section 2 summarizes the description of a dislocation itself, while the embedding in the boundary-value problem method is discussed in section 3. Section 4 provides a number of examples that demonstrate and verify the accuracy of the dislocation discretization separate from that of the finite-element correction for boundary problems. Finally, section 5 discusses the numerical accuracy of the finite-element method as it is used to enforce boundary conditions.

## 2. Dislocation model

The physical space is discretized as dislocations move on discrete glide planes. In our model physical space is described by defining the allowed glide systems and a spacing between glide planes, which is a multiple of the physical glide plane spacing.

The numerical implementation of three-dimensional dislocation dynamics must treat a number of issues. First, a discrete numerical representation of the dislocation must be created. Second, the smooth evolution of the dislocation must be numerically modelled. Finally, discrete events must be treated. Our implementation treats such discrete events as dislocation–surface intersections, the onset of cross-slip and the formation and dissolution of dislocation junctions. These are discussed in consecutive sections.

### 2.1. Discretization

The present discretization scheme belongs to the family of nodal models, where the dislocation line is interpolated between nodes. Different interpolation schemes have been proposed in the literature [6–8]. Here, the approach proposed by Kukta and Freund [6] is used and extended to include constrained nodes for junctions, cross-slip and dislocation–surface interactions. Figure 1 shows a discretized dislocation loop with Burgers vector  $\mathbf{b}$  on a glide plane with normal  $\mathbf{n}$ . The loop consists of a sequence of straight segments that are connected at nodes,

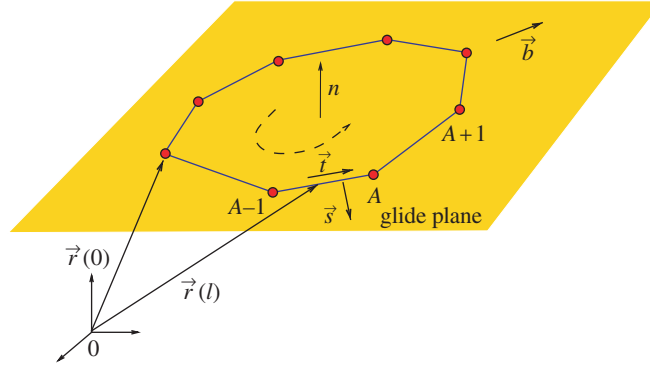


**Figure 1.** Description of a dislocation loop in its glide plane;  $\mathbf{n}$  is the normal vector of the glide plane; the orientation of the loop is given by the local tangent vector  $\mathbf{t}$  and the Burgers vector  $\mathbf{b}$ ;  $\mathbf{s}$  is defined as  $\mathbf{t} \times \mathbf{n}$ . A loop is confined to its glide plane.

marked as  $\{\dots, A-1, A, A+1, \dots\}$ . The degrees of freedom for the dislocation are the nodal positions  $\{\mathbf{r}_A\}$  and the velocities  $\{V_A\}$  ( $A = 1, \dots, N$ ) in the glide plane of the corresponding dislocation loop, where  $N$  is the number of nodes of the considered loop. The position along the dislocation loop  $\mathbf{r}(l)$  is parameterized by the curvilinear coordinate  $l$ . Thus the position of node  $A$  is  $\mathbf{r}_A = \mathbf{r}(l_A)$ , where  $l_A$  is its curvilinear coordinate.

In the model, a single dislocation loop is always associated with its glide plane; therefore, loops are flat (the handling of cross-slipped dislocations is explained in section 2.3.2). The time evolution of the dislocation microstructure is then given by the movement of the nodal points with velocities  $\{V_A\}$  (also in the glide plane). Climb is not considered here.

## 2.2. Dislocation dynamics

The dynamics of the dislocation structure is obtained in a framework that is equivalent to a one-dimensional finite-element method for each dislocation loop in the simplest case of a non-intersecting dislocation population with all nodes being material points. First, a general discussion of the instantaneous velocities is given, then the details of the force calculations, and finally the time evolution of the discretized dislocation structure is discussed.

**2.2.1. Nodal velocities.** We first consider nodes that are material points at the dislocation loop. The local dislocation velocity  $\mathbf{v}(l)$  at position  $\mathbf{r}(l)$  is then obtained by interpolation between the nodal velocities  $V_A$  of the two adjacent nodes, as expressed by

$$v_i(l) = \sum_{A=1}^N N_A(l) V_{Ai} \quad (i = 1, \dots, 3), \quad (1)$$

where  $V_{Ai}$  is the  $i$ th component of the nodal velocity  $V_A$ , and  $N_A$  is the linear shape function of node  $A$ .

At each point along the dislocation loop, the velocity is obtained from the local driving force. This driving force is the Peach–Koehler force, i.e. the configurational force on the dislocation. Postponing full discussion of the force calculation until section 2.2.2, note that for pure glide, only the component resolved in the glide plane,  $f^s$ , is of importance. The resolved Peach–Koehler force points in the direction  $\mathbf{s} = \mathbf{t} \times \mathbf{n}$ . The relationship between the Peach–Koehler force and dislocation velocity is controlled by atomic-scale (or smaller) processes that

are obviously not resolved in this model. Therefore, the relation has to be supplied through a constitutive rule. A common, semi-empirical law is (see e.g. [14, 15])

$$v_i(l) = V_T \left( \frac{f^s(l)}{\mu b} \right)^m \frac{f_i^s(l)}{f^s(l)}. \quad (2)$$

Here,  $f_i^s = f^s s_i$  is the  $i$ th component of the resolved Peach–Koehler force, which is computed from the stress field taking care of singularities as discussed in section 2.2.2. Furthermore,  $V_T$  is a temperature-dependent drag coefficient and  $m$  is the assumed power law exponent. For fcc crystals, a linear relationship ( $m = 1$ ) often suffices and is supported by arguments of phonon and/or electron drag (e.g. [18]). In that case,

$$f_i^s(l) = D v_i(l), \quad (3)$$

with  $D = \mu b / V_T$ . It is possible that  $V_T$  depends on the character of the dislocation (edge–mixed–screw), but as is usually done for fcc crystals [3, 16], this dependence is neglected here, and  $D$  is taken to be independent of  $l$ . Equations (2) and (3) should be satisfied at every point along the dislocation, i.e. for arbitrary values of  $l$ .

Following [6], the principle of virtual work is applied to the movement of the dislocation structure. With equation (3), the rate of energy dissipation due to dislocation glide becomes

$$\oint_L f_i^s(l) \delta v_i(l) dl = D \oint_L v_i(l) \delta v_i(l) dl, \quad (4)$$

where  $\delta v_i(l)$  is the virtual velocity of the dislocation at position  $l$  (summation over repeated vector/tensor indices, lower-case Latin letters, is implied). This velocity is interpolated from the nodal values,  $\delta V_{Ai}$ , by the same interpolation scheme (1), i.e.

$$\delta v_i(l) = \sum_{A=1}^N N_A(l) \delta V_{Ai}. \quad (5)$$

So far, the nodes defining a dislocation loop are material points of the loop. This is the default situation. In addition, we use so-called sliding nodes to treat dislocation junctions or dislocation segments leaving the crystal via a free surface. These nodes move with the material point of the dislocation but can also glide along the dislocation in order to satisfy certain constraints. The nodal velocities used in (1) and (5) have to be reconsidered for such nodes. The way in which the constraints are handled is illustrated in figure 2. In the case of a sessile junction, figure 2(a), the junction nodes, marked by  $\bullet$ , can only move parallel to the direction  $\mathbf{t}_{\text{glide}} = \mathbf{n}_2 \times \mathbf{n}_1$ , given by the intersection line of both glide planes with normal vectors  $\mathbf{n}_1$  and  $\mathbf{n}_2$ . Dislocations intersecting the specimen boundaries have surface nodes as shown in figure 2(b). These surface nodes are constrained to follow the intersection line of dislocation glide plane with the surface,  $\mathbf{t}_{\text{glide}}$  so that

$$\mathbf{V}_{A,\text{glide}} = V_A \mathbf{t}_{A,\text{glide}}, \quad (6)$$

where  $\mathbf{t}_{A,\text{glide}}$  is the prescribed glide direction of node  $A$ . Furthermore, for such nodes the interpolation scheme of equation (1) should include only the component of the velocity in the direction  $\mathbf{s}(l)$  see figure 1. This material nodal velocity is given by

$$V_{Ai} = P_{Aij}(l) V_{Aj,\text{glide}} = V_A s_i(l) s_j(l) t_{Aj,\text{glide}}, \quad (7)$$

where  $P_{Aij}$  is the projection operator at position  $l$  along the segment. To unify the notation this operator can be generalized to include the default material nodes as well:

$$P_{Aij}(l) = \begin{cases} \delta_{ij} & \text{for material nodes } A, \\ s_i(l) s_j(l) & \text{for sliding nodes } A, \end{cases} \quad (8)$$

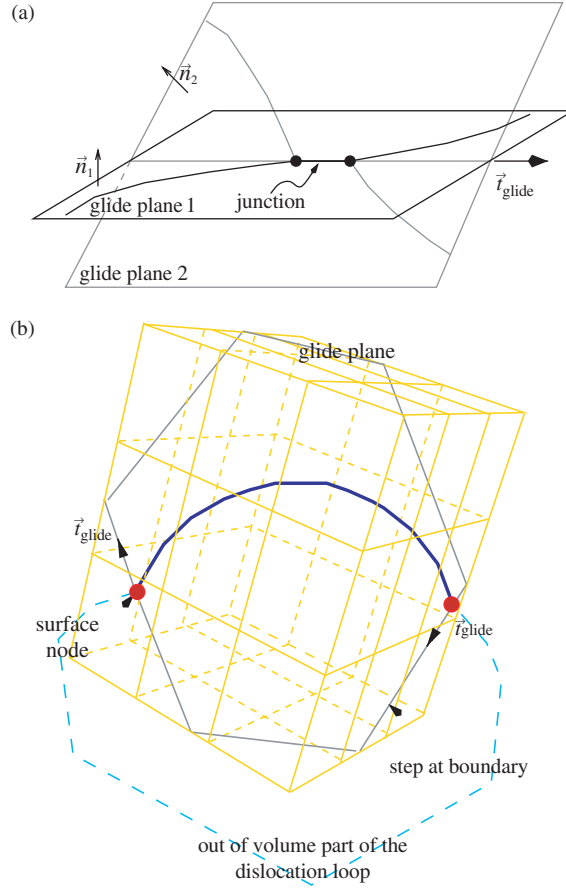


**Figure 2.** Possible restriction of nodal degrees of freedom: (a) two dislocations form a sessile junction; the allowed glide direction  $\vec{t}_{\text{glide}}$  is shown; (b) a dislocation sticks out of the volume; the surface nodes are restricted to move parallel to  $\vec{t}_{\text{glide}}$ ; the dislocation is closed outside the sample volume.

where  $\delta_{ij}$  is the Kronecker symbol. With a similar representation for the virtual velocity of sliding nodes, the virtual work condition (4) becomes

$$\sum_{A=1}^N \left[ \underbrace{\oint_L f_i^s(l) N_A(l) dl}_{F_{Ai}} - D \sum_{B=1}^N V_{Bj} \underbrace{\oint_L N_A(l) N_B(l) P_{Bjm}(l) P_{Ami}(l) dl}_{K_{ABij}/D} \right] \delta V_{Ai} = 0. \quad (9)$$

Requiring equation (9) to hold for arbitrary virtual velocities  $\delta V_{Ai}$ , we find

$$F_{Ai} - \sum_{B=1}^N K_{ABij} V_{Bj} = 0 \quad (i = 1, \dots, 3; A = 1, \dots, N), \quad (10)$$

as long as the  $N$  nodes are unconstrained. For the  $N_c$  constrained nodes, the combined equations (7) and (9) yield

$$\left( F_{Ai} - \sum_{B=1}^N K_{ABij} V_{Bj} \right) t_{Ai, \text{glide}} = 0 \quad (i, j = 1, \dots, 3; A = 1, \dots, N_c). \quad (11)$$

The nodal force  $F_{Ai}$  is in either case defined by

$$F_{Ai} = \oint_L f_i^s(l) N_A(l) dl \quad (12)$$

while the ‘stiffness’ matrix  $K_{ABij}$  in (10) and (11) is defined by

$$K_{ABij} = D \oint_L N_A(l) N_B(l) P_{Aim} P_{Bmj} dl. \quad (13)$$

As in a standard finite-element representation, the linear interpolation function  $N_A(l)$  limits the domain of integration in (12) and (13) to the segments sharing node  $A$ . Noting that  $f_i^s(l) = f^s s_i$ , we can write the nodal force as

$$F_A = s_{A-1,A} \int_{A-1}^A f^s(l) N_A(l) dl + s_{A,A+1} \int_A^{A+1} f^s(l) N_A(l) dl, \quad (14)$$

where  $s_{A-1,A}$  is the in-plane unit normal vector to the segment with endpoints  $A-1$  and  $A$  (see figure 1).

The final system of equations formed by the set of equations (10) and the set of equations (11) and (6) for the sliding nodes is then solved for the nodal velocities  $V_{Ai}$ . Very high nodal velocities may occur due to some unrelaxed dislocation geometries, which might occur after discrete events as loop intersections and formations of junctions. To improve the numerical stability, a cut-off velocity is used, which is high enough ( $1/10$  to  $1/2$  of the shear wave velocity) not to affect the overall response.

**2.2.2. Evaluation of nodal Peach–Koehler force.** The computation of the nodal forces,  $F_{Ai}$ , from (14) requires physical approximations for the singular stress field along dislocation lines and careful numerical integration. There are two basic contributions to the Peach–Koehler force,  $f^s$ , at any point: first,  $\tilde{f}^s$  due to the stress fields of all dislocations including the self interactions; second,  $\hat{f}^s$  due to image forces and boundary conditions. The discussion of  $\hat{f}^s$  is given in section 3.1.

The long-range dislocation contribution,  $\tilde{f}^s$ , can be decomposed into a sum over all dislocations of the Peach–Koehler force due to a single dislocation  $m$ ,  $\tilde{f}_{(m)}^s$ . The first term in equation (14), therefore, has a dislocation–interaction contribution

$$\sum_m \int_{A-1}^A \tilde{f}_{(m)}^s(l) N_A(l) dl = \sum_m \sum_{S=1}^N \int_{A-1}^A \tilde{f}_{(m,S)}^s(l) N_A(l) dl, \quad (15)$$

which can be further decomposed into contributions per segment  $S$  of each dislocation  $m$ , as shown in (15). The integrals in equation (15) are performed numerically. By default, one integration point is used, which is located in the centre of the segment  $(A-1)-(A)$ . The term  $\tilde{f}_{(m,S)}^s$  in (15) is evaluated using Brown’s normalization scheme [17] for the case where  $m$  is the same as that of the dislocation under consideration and  $S$  is contained in the neighbourhood of segment  $(A-1)-(A)$ , as shown in figure 3. Brown’s scheme allows the self-stress of a dislocation to be computed as the average stress of two laterally displaced segments. The chosen lateral splitting displacement,  $\rho = b-3b$ , is validated in sections 4.1 and 4.2 for the example of a circular loop and the critical activation stress for a Frank–Read source by comparing to analytical models using a different cut-off scheme. Brown’s splitting and averaging procedure is also applied for neighbouring segments which are closer than a critical distance or which have a tangent direction almost parallel to the considered segment as shown in figure 3. In the latter case, a numerical singularity is removed. A typical geometry with several collinear segments is the initial configuration of a Frank–Read source. This initially

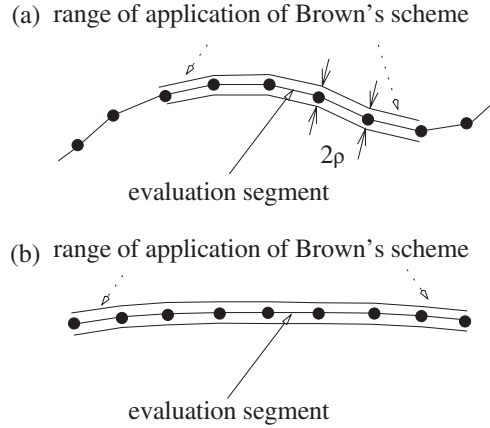


**Figure 3.** The Brown scheme is applied around the central element. Two conditions control the extension of the splitting region: (i) the distance of the interacting segment to the evaluation point and (ii) the angle between the two segments. The segments within the splitting region are moved in the glide plane to the new position. The distance between the splitted nodal points is  $2\rho$ . This splitting region is shown for two cases (a) evaluating the stress at the integration points of the marked segment of a dislocation loop; (b) Frank–Read source under small applied stress; the segments are almost aligned (small angle between the segments); therefore the Brown scheme is applied along the whole dislocation source.

straight dislocation is discretized by several segments in order to allow the dislocation to bow out as shown in figure 3(b).

The need for special numerical treatment of the dislocation self-interaction is evident from the study to be presented in section 4. The number of integration points per segment needs to be increased in order to capture the self-stress contribution adequately. This need arises because the discretization scheme localizes the curvature to the nodal points. The sudden change of segment orientation causes a strong variation of the Peach–Koehler contribution  $\tilde{f}_{(m,S)}^s$  close to the nodal points. This strong variation has to be captured in the calculation of the nodal forces. Therefore, the calculation of the contribution of the segments included in Brown's regularization scheme is done using a larger number of integration points per segment. It will be demonstrated in section 4 that this procedure converges.

The drawback of this method is the increased number of stress-field evaluations even though the variation of the field is essentially known. The variation of the Peach–Koehler force caused by the neighbouring segments,  $\tilde{f}_{(m,S)}^s$ , is essentially of the form  $1/(r + a_0)$  towards both endpoints of the considered segment, where  $r$  is the distance from an endpoint and  $a_0$  is on the order of the splitting distance  $\rho$ . Therefore, it is computationally advantageous to fit this functional behaviour to each half of the considered dislocation segment to a few evaluation points only.

**2.2.3. Time-stepping and evolution.** The evolution of the dislocation configuration is traced by integration in time, using an explicit Euler scheme with time step  $\Delta t$ . The time step is determined in an adaptive manner so that control of the local evolution of the dislocation microstructure is ensured. Two conditions on local changes of the dislocation geometry are used to determine the time step: (i) the maximum length change for each dislocation segment is limited to a fraction of its initial length; two parameters are used: one for shrinking and one for growing segments; (ii) the rotation of a segment during a time step is limited to a critical value,  $\alpha_{\text{crit}}$ . Condition (ii) is relaxed for segments that have a surface node or whose neighbour has

a surface node because simulations have shown that these segments rotate relatively rapidly and would lead to an unnecessarily small time step. Therefore, somewhat larger rotations are permitted for these segments.

While trying to assess the appropriate parameter values for (i) and (ii), it has been found that it is condition (ii) on rotation that limits the time step. The maximum allowed angle  $\alpha_{\text{crit}}$  has to be chosen carefully and dependent on the state of the segment. Dislocation configurations at or close to equilibrium tend to have nodes that fluctuate. These fluctuations involve rotations of the segments and have to be limited. This suggests that a small  $\alpha_{\text{crit}}$  should be used. For the opposite case, e.g. a Frank–Read source driven at over-critical stress, the nodes forming the source are not fluctuating, thus allowing for much larger time steps. To take into account both cases, the following two-step procedure has been developed:

1. Calculation of all dislocation–dislocation interactions, including the detection of possible intersections of dislocations. The boundary conditions are updated after adding to the physical time  $t$  of the last step the global time step  $\Delta t$ , which is the sum of the sub-time-steps  $\delta t$  calculated in step 2. Initial values are used at the first evaluation of step 1.
2. Determination of a sub-time-step  $\delta t$  and movement of the dislocation microstructure followed by a test for topological changes. This procedure includes local recalculation of interactions. The following sub-steps 2(a)–(d) are repeated until condition 2(c) is satisfied:
  - (a) Calculation of the maximum sub-time-step  $\delta t_A$  for each segment, on the basis of the conditions for segment length change and rotation. Extraction of the sub-time-step  $\delta t$  from the ensemble of  $\{\delta t_A\}$  as described subsequently.
  - (b) Updating of entire dislocation structure over  $\delta t$ . Topological changes are performed, e.g. formation of junctions, cross-slip, and surface intersection.
  - (c) After either having reached the maximum number of repetitions of step 2, which is a parameter, or having moved the dislocation in step 2 during more than e.g.  $10^{-9}$  s, go back to step 1, otherwise proceed with sub-step 2(d).
  - (d) The Peach–Koehler force on loops that have changed topology are completely recalculated. For the remaining loops only the local interactions are updated (i.e. those given by the contribution of segments included in the Brown’s scheme and the interactions with segments that are candidates for intersection). Return to sub-step 2(a).

The time-step calculation in point 2(a) contains some further exception handling to increase the global time step  $\Delta t$ . It has been found that the distribution of time steps  $\delta t_A$  is rather broad and has a long sparsely populated tail of small time steps. In each simulation step, a few nodes need an extremely small time step ( $\approx 10^{-13}$  s) while all other nodes allow for time steps one or more orders of magnitude larger. Small time steps are needed for nodes that fluctuate around equilibrium positions, even though these motions do not contribute to deformation. Small time steps are also found for regions where the discretization has been refined due to a higher local dislocation density, leading to intersections. The sub-time-step  $\delta t$  is therefore taken to be the smallest value of the nodal time steps  $\{\delta t_A\}$  after exclusion of the fraction of nodes having the smallest local time steps. This fraction is specified for the applications shown later. A further condition is used to ensure that the time step remains reasonably large (on the order of  $10^{-11}$  s): the time step  $\delta t$  is not allowed to drop under a fraction 0.01–0.1 of the average sub-time-step.

In point 2(b) the dislocation configuration is updated using explicit Euler integration, i.e.

$$\mathbf{r}_A(t + \delta t) = \mathbf{r}_A(t) + \mathbf{V}_A(t) \min(\delta t_A, \delta t). \quad (16)$$



The minimum value of  $\delta t_A$  or  $\delta t$  is needed for those nodes that were either excluded from  $\{\delta t_A\}$  or subjected to the condition which assures that the decrease of the sub-time-step is limited.

The main reason for applying a two-level time stepping approach is a reduction in the calculation time due to the fact that for most of the loops only local interactions are recalculated during sub-time-steps. This minimizes the  $N^2$  problem of interaction calculations, without jeopardizing the accuracy, since rapidly varying interactions are recalculated on smaller time intervals than slowly varying interactions.

**2.2.4. Adaptive dislocation re-discretization.** As the dislocation structure evolves, nodal movement changes the discretization of the individual dislocation loops in several respects: the length of segments, the local curvature and the nearest neighbour environment are altered. Therefore, it is necessary to re-discretize the dislocations at regular intervals. This re-discretization procedure relies on the following considerations:

- (i) the level of refinement of the discretization depends on the local curvature of the dislocation;
- (ii) the length of segments should be in a predefined range  $[l_{\min}, l_{\max}]$ ;
- (iii) the allowed length of a segment depends on its neighbourhood.

With respect to the first of these, simulations have shown that a circular dislocation loop is discretized with satisfactory accuracy by using  $N_{\text{circ}} = 20$  segments. The number of integration points per segment is adapted to the segment length, such that the distance between the nodal points and the closest integration point is about  $\sqrt{2}b$ . This is necessary for an accurate self-force calculation (see section 4.1). A first guess for the total number of segments for an arbitrary dislocation loop is then be obtained from

$$n = \frac{\omega}{2\pi} N_{\text{circ}}, \quad (17)$$

where  $\omega = \oint |\kappa(l)| dl$  is the line integral of the absolute value of the local curvature  $\kappa(l)$  along the dislocation loop. This initial number of nodes is adapted on the basis of the following set of rules:

1. The number  $n$  is compared to the initial number of nodes  $n_0$  in the loop; the change in the number of nodes is limited to 50%.
2. For very short dislocation loops the number of nodes is given by the total length of the dislocation divided by the minimum length  $l_{\min}$  rounded down to the nearest integer. Furthermore, the absolute minimum allowed number of segments is three.
3. From the condition for the maximum length of a segment, the minimum number of segments needed for the loop is calculated and used as a new value for  $n$  if the previously obtained value is smaller.
4. For parts of a dislocation loop between two junctions, the minimum number of segments is set to be five. This allows the dislocation to bow out under the applied stress.

Once the number of nodes is determined, the following method has been chosen to place these nodes along the dislocation line. First, the entire dislocation length is fitted with a cubic spline. The redistribution of nodes is based on both the segment length and the local curvature. This is carried out by positioning consecutive nodes,  $A$  and  $A + 1$ , at coordinates  $l_A$  and  $l_{A+1}$  such that

$$w(l_A, l_{A+1}) = \int_{l_A}^{l_{A+1}} |\kappa|^\alpha \sqrt{(x'(l))^2 + (y'(l))^2} dl \quad (18)$$

is approximately constant along the dislocation. Here,  $(x(l), y(l))$  are the in-plane coordinates of the spline interpolation, a prime denotes the derivative with respect to the arc-length  $l$ , and

$\alpha$  is a weighting exponent. For  $\alpha = 0$  an equal length of the segments is imposed. With increasing  $\alpha$  the density of nodes increases with local curvature. In the simulations to be presented later,  $\alpha$  was chosen between 0.2 and 0.75.

The condition (ii) above forces the segments to have a length between the minimum value  $l_{\min}$  and the maximum value  $l_{\max}$ . These two values have to be chosen in relation to the desired resolution for geometrical reaction. Strong local curvature may lead to segments shorter than  $l_{\min}$ . This is tolerated but generally gives rise to frequent re-discretization of that loop.

Finally, information is used about the neighbourhood of each dislocation segment. For each segment we know the minimum distance to possible intersecting segments in the same glide plane, on inclined glide planes and to segments in parallel glide planes. Resolving such interactions requires a local dislocation discretization using segments that have a length comparable to these minimum distances. Therefore, some nodes have to be inserted between the newly distributed nodes as described above.

The actual placement of new nodes at the determined curvilinear positions along the dislocation,  $\{l_A\}$ , requires special attention. As the dislocation is taken to be an ensemble of connected straight segments, the new positions given by the curvilinear coordinates  $\{l_A\}$  of the spline interpolation will not be located on the initial dislocation loop. To avoid artificial changes of the loop geometry, a three step procedure is established. New nodes are placed at the corresponding coordinates of the straight segments. The dislocation contains the old and new nodes and the geometry corresponds to the initial one. In a second step, the new nodes are then moved to the positions given by the spline under the condition that no intersection of the considered dislocation loop with other dislocations takes place. Finally, old nodes are removed using the same condition.

In order to avoid artificial movement of the dislocation this procedure is only used for dislocation loops that give rise to a sufficiently small time step. For a population of dislocations, it is found that only a few loops require such small time steps, while most other loops allow for much larger time steps. Full re-discretization using all three considerations (i)–(iii) listed at the beginning of this section is only applied to loops with small time steps. The refinement procedure (iii) is applied to all loops, independent of the maximum time allowed by the loop, in order to ensure that local interactions are traced correctly.

### 2.3. Discrete events

In addition to the continuous dynamic evolution of dislocations, there are also discrete events that must be incorporated into the model. Here, junction formation, junction propagation, junction dissolution and cross-slip are discussed. Discussion of dislocation–boundary intersections is deferred to section 3 where implementation of boundary conditions is explained.

*2.3.1. Detection and classification of junction formation.* The formation of junctions needs special attention. In the implementation, information about segments that may lead to the formation of junctions is collected prior to each new time step. Possible detection of junctions is an  $N^2$  problem in computational time as, in principle, all segments have to be tested against one another for possible intersections. In the literature [3], box search algorithms have been proposed to reduce the search time. At the current stage of development, a different approach is taken. During the evaluation of the dislocation–dislocation interactions, the possibility of two segments encountering each other is tested using the available distance information. The detection is subdivided into two possible types of intersection: (i) with segments in the same glide plane and (ii) with segments of forest dislocations.

For segments on the same glide plane, a tree data structure with possible candidates for intersections is built using the minimum distance between the segments as an order parameter. After the movement of the dislocations, this tree is iteratively searched. Intersections are tested for, starting from the closest two possibly intersecting segments. Segments closer than a critical distance or segments that have intersected are reconnected taking into account the local dislocation orientations and the Burgers vectors.

The second type of intersection involves forest dislocations on different glide systems. During the evaluation of the dislocation–dislocation interactions, a test of possible intersection of these segments is performed based on the relative position of the segments and glide planes. This information is stored in a second tree structure that is evaluated after the movement of the nodes, starting from the closest two possibly intersecting segments. Whether or not to form a junction is determined by both an energetic and a geometrical criterion. The following approximate expression for the elastic energy of dislocation per unit length is used for the energetic criterion [18]:

$$\frac{E(\mathbf{b}, \mathbf{t})}{L} = \frac{\mu}{4\pi} \left( (\mathbf{b} \cdot \mathbf{t})^2 + \frac{|\mathbf{b} \times \mathbf{t}|^2}{1 - \nu} \right) \ln \frac{R}{\rho}, \quad (19)$$

where  $\mathbf{t}$  is the dislocation line direction and  $R$  is some arbitrary large-scale cutoff. The condition for the formation of a junction between parallel dislocation segments with Burgers vectors  $\mathbf{b}_1$  and  $\mathbf{b}_2$  reads

$$E(\mathbf{b}_1, \mathbf{t}) + E(\mathbf{b}_2, \mathbf{t}) > E(\mathbf{b}_1 + \mathbf{b}_2, \mathbf{t}), \quad (20)$$

with  $\mathbf{t}$  the line direction of the junction. The orientation of the loop has to be taken into account during the calculating of the total Burgers vector  $\mathbf{b}_1 + \mathbf{b}_2$  when evaluating  $E(\mathbf{b}_1 + \mathbf{b}_2, \mathbf{t})$ .

The geometrical condition for testing the formation of a junction is shown in figure 4. The segment intersection is detected by a change in sign of  $\mathbf{k}$ , the vector pointing from segment 1 to segment 2 along the intersection line of the two glide planes. The intersection line has the

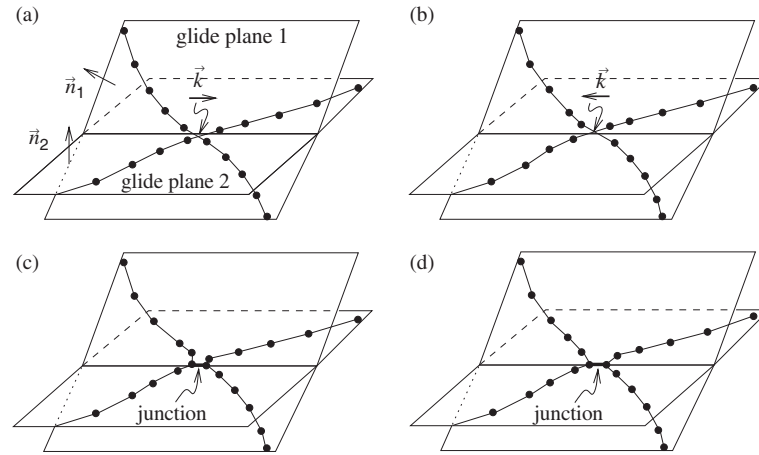


**Figure 4.** The formation of a junction: (a) before the formation; the vector  $\mathbf{k}$  is parallel to the intersection line of glide planes 1 and 2 and indicates the direction the relative position of segment 1 (in glide plane 1) to segment 2 (in glide plane 2); segments 1 and 2 have been detected as possibly intersecting segments; (b) configuration of junction formation detection:  $\mathbf{k}$  points in opposite direction of configuration (a); an ‘overshooted’ geometry occurs; (c) geometry imposed due to junction formation; (d) relaxation of imposed junction geometry in the following time steps. Note that the geometries have been exaggerated for clarity.

direction  $\mathbf{n}_1 \times \mathbf{n}_2$ , where  $\mathbf{n}_1$  and  $\mathbf{n}_2$  are the unit normal vectors of the two glide planes. The figure shows the sequence prior to detection (a), the detection (b) and the imposed initial configuration of the junction (c). The junction segment is placed along the intersection line. The endpoints are connected to the corresponding dislocations in the two glide planes as shown in figure 4(c). The initial junction length is set to be one-third of the length of the shorter intersecting segment. The junction length is chosen to be finite to avoid numerical problems arising from zero-length segments, but small enough to avoid distorting the local configuration too greatly. Unfortunately, this leads to an overshoot of the ideal ‘relaxed’ junction configuration. However, this procedure allows the use of larger time steps compared to a careful and slow approach of the two segments until formation of the junction, while maintaining sufficient accuracy. As the formation of the junction involves some local rearrangements, dissolution of the loop is prohibited during the following four time steps. During these time steps, the configuration can relax to that shown in figure 4(d).

Once formed, junctions can evolve in time. As mentioned in section 2.2.1, the nodes comprising the endpoints of the junction are constrained to move along the junction line direction  $\mathbf{k}$  as prescribed by equation (6). In addition to this smooth form of propagation, the junction can propagate if the two branching segments attached to the end-node collapse along the junction line direction. This event is ‘detected’ if these segments are within  $8^\circ$  from the junction line, which is considered parallel from the numerical point of view (the result is not sensitive to this angle).

Finally, it is necessary to apply rules for junction dissolution. The junction is dissolved if its length shrinks to less than a critical length of the order  $1-5b$ .

Explicitly forming the junction in the simulation has numerical advantages over allowing the junction to behave as two separate dislocation segments, i.e. allows greater time steps. It is unclear at this moment whether the proposed rules will give behaviour different from that found in other simulations [5, 9].

**2.3.2. Cross-slip.** Another type of discrete event treated in the model is cross-slip. Cross-slip is a thermally activated process, which has to be included in order to handle phenomena such as dynamic recovery. The exact constitutive rules for cross-slip are not well known. The rules from [4] are used here because they take into account most aspects of cross-slip initiation while being at the same time easy to implement. In the present implementation, cross-slip is treated as a junction with zero total Burgers vector. This allows the cross-slipped loop to be handled as two distinct loops with opposite Burgers vectors or tangent directions that lie on separate but intersecting glide planes and that share a common screw segment. The cross-slip procedure involves two steps: the first step determines the screw dislocation parts that may potentially cross-slip; the second step applies the detailed cross-slip condition.

The first step involves the identification of the segments that may potentially cross-slip. Each dislocation loop is searched for a sequence of segments which show almost screw character. The character of each segment is quantified by

$$C = \frac{\mathbf{n} \cdot (\mathbf{b} \times \mathbf{t})}{b}, \quad (21)$$

so that  $C = 0$  for pure screw segments and  $C = \pm 1$  for pure edge segments. A change of sign of this quantity between two neighbouring segments indicates a pure screw dislocation part. Starting from these two segments, sequences of segments on either side are identified which are oriented within  $10^\circ$  from the screw orientation as done in [4]. From this sequence, the length  $L$  of the cross-slipping dislocation part is determined. Since the sequence of nearly screw segments may traverse many possible cross-slip planes, the glide plane closest to the centre

of gravity of the segments is chosen as the actual cross-slip plane. The initial cross-slipped dislocation is straight and can only glide in the cross-slip plane.

Next it is decided whether or not cross-slip actually takes place. The first set of rules to handle the onset of cross-slip is taken from [4]:

- the average Peach–Koehler force on the segments that may potentially cross-slip projected on the new glide plane must be larger than the projection on the original glide plane;
- the probability of cross-slip during a time increment  $\delta t$  is then given by

$$P(L) = \frac{\beta L \delta t}{L_0 \delta t_0} \exp \left( -\frac{V_{\text{act}}}{kT} (|\tau| - \tau_{\text{III}}) \right),$$

where  $\beta$  is a normalization constant,  $V_{\text{act}}$  an activation volume, and  $\tau_{\text{III}}$  is the stress at which stage-three hardening starts. Furthermore,  $L_0$  and  $\delta t_0$  are reference values for the length of the cross-slipping segment and for the time step. In aluminium, the values are chosen such that there is a probability of one for two opposite screw dislocations of length  $L_0 = 1 \mu\text{m}$  at a distance of  $1 \mu\text{m}$  to cross-slip in  $\delta t = \delta t_0 = 1 \text{ s}$ :  $\beta = 10^5$ ,  $\tau_{\text{III}} = 5 \text{ MPa}$  and  $V_{\text{act}} = 300b^3$  [3, 4, 23].

This type of condition reflects the thermal activation of cross-slip, expressed in terms of the probability function. In early trials with the present model, it was observed that this procedure can create unstable cross-slip dislocations configuration, which are not of interest in a mesoscopic simulation. Therefore a stability test is applied to the cross-slipped segments by requiring the Peach–Koehler force  $f_{\text{CS}}^s$  in the cross-slip plane to be sufficiently large. The required value of  $f_{\text{CS}}^s$  is taken to be compared with the known critical force  $b\sigma_{\text{cr}}$  to activate a Frank–Read source of the same length  $L$ . The cross-slipped configuration is considered to be stable for  $f_{\text{CS}}^s > 0.1b\sigma_{\text{cr}}$ . The implications of this ratio bear further testing; other rules can be readily implemented.

### 3. Method for boundary-value problems

In 1995, Van der Giessen and Needleman [11] introduced a general method for the incorporation of boundary conditions in a discrete dislocation framework. This method is able to handle arbitrary boundary conditions such as specified tractions or displacements, periodicity, or mixed conditions. Previous applications were in two dimensions only [11, 16, 21, 22]. Here, details of the implementation for three dimensions are discussed.

#### 3.1. The decomposition

The discussion in the previous section has bypassed the question of how the Peach–Koehler force is calculated. In the class of dislocation models under consideration this requires the solution of the relevant elasticity problem, one that is extremely difficult because of the line singularities representing the dislocations. Only in exceptional cases is the exact solution known in closed form. For example, for a linear elastic isotropic material, the stress [6, 18, 19] and displacement fields [20] for dislocation loops described by a sequence of straight dislocation segments in infinite space are known. These solutions give an accurate description of the singular behaviour close to the dislocation (up to a few Burgers vectors away from the core to avoid nonlinear elastic effects) but are not necessarily consistent with the boundary conditions on a finite sample of material.

To find the elastic fields consistent with appropriately prescribed boundary conditions, the method of [11] is used. The key idea is to use superposition to correct infinite-space fields with

an ‘image’ field to satisfy the boundary conditions. Denoting the infinite-space fields with a superposed ( $\sim$ ) and the finite-element correction image fields with ( $\hat{\cdot}$ ), the stress, strain and displacement components are expressed as

$$\sigma_{ij} = \tilde{\sigma}_{ij} + \hat{\sigma}_{ij}, \quad \epsilon_{ij} = \tilde{\epsilon}_{ij} + \hat{\epsilon}_{ij}, \quad u_i = \tilde{u}_i + \hat{u}_i, \quad (22)$$

respectively. The ( $\sim$ )-fields are the superpositions of the fields of individual dislocations. The image fields give rise to  $\hat{f}^s$ , mentioned in section 2.2.2. With the discretization of a dislocation as discussed in the previous section, the latter fields of individual dislocations are the sum of the fields of straight dislocation segments in infinite space. For these, the expressions given in [19] for the stress fields and in [20] for the displacement fields are used. The ( $\hat{\cdot}$ )-fields are to be determined such that the tractions  $\hat{T}_i = \hat{\sigma}_{ij}n_j$  satisfy

$$\hat{T}_i = T_i^0 - \tilde{T}_i, \quad \tilde{T}_i = \tilde{\sigma}_{ij}n_j \quad (23)$$

on that part of the surface where tractions are prescribed to be  $T_i^0$ , and

$$\hat{u}_i = U_i^0 - \tilde{u}_i \quad (24)$$

on that part of the surface where displacements are prescribed to be  $U_i^0$ . Thus, the singular part of the fields due to the dislocations is captured by the ( $\sim$ )-fields, while the ( $\hat{\cdot}$ )-fields are smooth, as long as the dislocations are sufficiently far away from the surface. Therefore, the image solution of the elasticity equations subject to the boundary conditions (23) and (24) can be obtained accurately by numerical methods for such configurations. However, when dislocations come very close to the surface or even intersect the surface, the finite-element method may no longer be able to resolve the ( $\hat{\cdot}$ )-fields accurately. An assessment of the accuracy of this method is given in section 5. As will be seen, these issues are much more complicated in three dimensions than in two.

### 3.2. Numerical solution of image fields

A standard finite-element method is used to obtain the ( $\hat{\cdot}$ )-fields. In two dimensions, simple four-node quadrilateral elements have been found to be convenient and sufficiently accurate [16, 21, 22]. However, the use of higher-order elements is advantageous in three dimensions. We use 20-node quadratic elements with eight-point Gaussian integration for the stiffness matrix. Two critical ingredients for the implementation are: (i) applying the correct boundary conditions to obtain the proper ‘image’ fields, and (ii) extracting a smooth continuous stress field from the finite-element solution.

**3.2.1. Boundary conditions.** Displacement boundary conditions, equation (24), are incorporated directly as prescribed nodal displacements  $\hat{u}_i$ . Traction boundary conditions, equation (23), are incorporated as prescribed nodal forces, determined in a work-equivalent manner. This requires integration of  $(T_i^0 - \tilde{T}_i)\delta\hat{u}_i$  over the surface of an element, with  $\delta\hat{u}_i$  the components of the virtual displacement field. The precision with which the integration needs to be performed depends strongly on the behaviour of  $\tilde{T}_i = \tilde{\sigma}_{ij}n_j$  on this surface. If a dislocation is near the surface, the proximity of the singularity requires the integration to be carried out using a sufficiently large number of integration points. Tests to be discussed later suggest the use of up to  $10^2$  Gauss integration points per surface element (a surface element is the face of a finite element located at the surface).

**3.2.2. Stress field extraction.** Once the finite-element problem is solved, resulting in a set of known finite-element node displacements,  $\{\hat{u}_i\}$ , the stress field,  $\hat{\sigma}_{ij}$  must be determined

throughout the volume. Unfortunately, the stress field obtained directly from the finite elements are discontinuous over element borders and therefore might trap dislocations at the finite-element boundaries. To obtain a continuous stress field throughout the volume, the following smoothing procedure is adopted:

1. The stress field is evaluated at the eight integration points of each element.
2. For each element, the stress field at the integration points is extrapolated to the eight corner nodes of the 20-node element. This extrapolation is accomplished using the first-order shape functions for eight-node bricks. The final nodal value is averaged over the different contributions from all elements sharing the same node.
3. The eight-node shape functions are then used to obtain  $\hat{\sigma}_{ij}(x_k)$  for arbitrary positions  $x_k$  in the volume on the basis of these nodal values in the corners. This finally results in a continuous stress field.

A similar extrapolation can be carried out based on the 20-node interpolation function and will be compared with the eight-node approach in section 5.1. Unless specified otherwise, the eight-node scheme is used in the calculations.

### 3.3. Dislocation–boundary intersections: the concept of virtual dislocations

The evolution of the dislocation structure may lead to events where nodal points and part of the corresponding dislocation segments leave the material. These events need to be detected when nodes are moved and proper constraints must be applied to the resulting surface nodes. To facilitate this detection, the surface of the sample is approximated by a triangular mesh. Thus the surface becomes locally flat. The further handling of such events is governed by the following basic considerations. The dislocation loop is divided into a part that is inside the material and a part that has left the material. The latter part is called the virtual dislocation because it serves only a computational purpose. Strictly speaking, the analytic expressions for the stress fields of a dislocation in an infinite material is only valid for closed dislocations, and the displacement field is ill defined unless the dislocation loop is closed [18]. Thus, only closed loops can be used for the calculation of the ( $\sim$ )-fields and the virtual segments of the dislocation are necessary. The configuration of the virtual part of the dislocation can be chosen arbitrarily: the ( $\wedge$ )-fields will ensure satisfaction of the boundary conditions. However, a judicious choice of this configuration can aid the calculation of the dislocation–surface interaction.

When part of a dislocation loop leaves the material, a step is left at the surface between the two exit points. These parts are separated by surface nodes that are restricted to move along the triangulated surface. The constraint of the dislocation nodes on the surface, expressed in equation (11), is strictly valid as long as the nodes remain on the original surface triangle. When a surface node leaves its initial triangle, the node can find itself either inside the volume, on the surface, or outside the volume, depending on the local curvature of the surface. The intersection of the dislocation line with the new surface triangle is computed using connectivity information of the surface triangles. Note that the approximate representation of a convex or concave surface introduces an error in the energy dissipation rate, equation (9), but the error is negligible considering that the length of the involved dislocation segment is much smaller than the total dislocation length.

An important issue that has not received much attention in the literature, except in [6], is how the external virtual part of the dislocation is handled, since this is not a real material defect. When solving boundary-value problems, it is in general necessary to preserve the surface steps produced by the dislocation parts that have left the volume. There is some freedom in how this is implemented, but care needs to be taken that the strong attractive image force on the

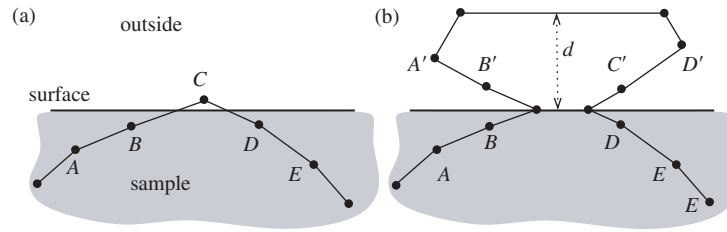


**Figure 5.** The pseudo-mirror construction applied in the simulation to mimic the attractive interaction: (a) node leaves the sample; (b) surface nodes are introduced and a mirror construction is created. The view shows the projection onto the glide plane.

remaining dislocation from the free surface is resolved to sufficient accuracy. This attractive image force is included in the ( $\sim$ )-fields obtained by the finite-element method. The spatial resolution of a finite-element discretization is often much coarser than the Burgers vector  $\mathbf{b}$ , so that the short-range interaction around the exit point of the dislocation (surface node) is not captured and corrected by the finite-element image solution. On the other hand, refining the finite-element mesh to near-atomic-level resolution is usually not practical.

The short-range stress field corrections are approximated using the extra degrees of freedom of the virtual segments. In simple cases (for plane surfaces and dislocation lines parallel to that surface) [18] the attractive interaction force is known in closed form using the dislocation image construction; the idea of image dislocations is used in this simulation. Therefore, the virtual dislocation is needed to construct such an image dislocation. As the expressions for the ( $\sim$ )-stress and displacement field are valid for plane dislocation loops only, the mirror construction is carried out in the glide plane of the intersecting loop. The first two outer segments (after a surface node) are put into positions which correspond to a ‘mirror-image’ of the inner last two segments before the surface node as shown in figure 5. The distance of the nodes  $A$  and  $B$  to the intersection line of the glide plane with the surface are  $d_A$  and  $d_B$ ; the outer mirror nodes  $A'$  and  $B'$  are at distances of  $1.1d_A$  and  $1.2d_B$  from that line. The pre-factors 1.1 and 1.2 are chosen to increase the distance of the outer nodes in case the inner segments are almost parallel to the surface. The positions of the nodes  $C'$  and  $D'$  are obtained in the same way. This procedure determines the positions of the first and last two outer segments. The outer dislocation loop is closed in a smooth manner by projecting the intermediate points to a given distance  $d$  from the surface in the glide plane of the dislocation. This distance  $d$  varies with the considered shape and size of the specimen. For each application in section 4 this value is generally specified to be of the order of  $10^3 a$ , where  $a$  is the lattice parameter of the material. Using this ‘mirror-image’ construction does not give correct short-range stress fields, but it does preserve the strong dislocation–surface attraction with little computational cost. Loops that have left the volume completely, leaving a step at the surface, are kept at the distance  $d$  and are included in the dislocation interaction calculation.

#### 4. Validation: dislocation discretization

In this section, the methods used to model discrete dislocation dynamics are validated in an infinite solid for a few simple cases. These examples include calculation of the force to collapse a circular loop, the operation of a Frank–Read source, and the formation of a Lomer lock. The performance of the boundary-value problem formulation is given in section 5.



#### 4.1. Circular loop

In the first example a circular dislocation loop in an infinite solid is considered. This configuration allows a comparison of the model with an analytical solution for the resolved shear stress valid in the limit of large  $R/\rho$ , where  $R$  is the radius of the loop and  $\rho$  is the splitting distance [6]. The nodal forces computed by the simulation are compared with the nodal forces computed by integrating the analytical solution over the segments, leading to

$$F_A^{\text{circ}} = -\frac{\mu b^2}{8\pi} \left[ \frac{2-\nu}{1-\nu} \ln \left( \frac{8R}{\rho} \right) \Delta\theta + \frac{\nu}{\Delta\theta(1-\nu)} \left( 3 \ln \frac{8R}{\rho} - 8 \right) \sin 2\theta \sin^2 \Delta\theta \right]. \quad (25)$$

Here,  $\mu$  is the shear modulus  $\nu$  is Poissons ratio  $\theta = \mathbf{t} \cdot \mathbf{b}/b - \pi/4$ , where  $\mathbf{t}$  is the tangent direction at the considered nodal point, and  $\Delta\theta = 2\pi/n$ , where  $n$  is the number of nodes or segments used to discretize the circle.

The two main parameters influencing the accuracy in calculating the nodal forces are the number of segments used to discretize the loop and the number of Gauss integration points per segment. Increasing both numbers improves the agreement between the nodal forces computed using the simulation and the analytical approximation (25), as shown in figure 6. Convergence towards the analytical approximation shows that the discrete representation of the circular loop does not have a significant affect on the nodal Peach–Koehler force experienced by the loop.

From this test, a criterion for the approximate number of integration points needed for the desired accuracy is obtained; the first and last integration point on each segment should be approximately  $\sqrt{2}b$  from the nodal point.

The splitting distance in the analytical expression and in the calculation are set equal. The influence of varying  $\rho$  on the relative error is small for the tested range of  $\rho \in (b, 3b)$ .

#### 4.2. Frank–Read source

The next example is a Frank–Read source. Here, the relevant quantity is the critical stress needed to produce dislocations from a Frank–Read source. We compare the results of our

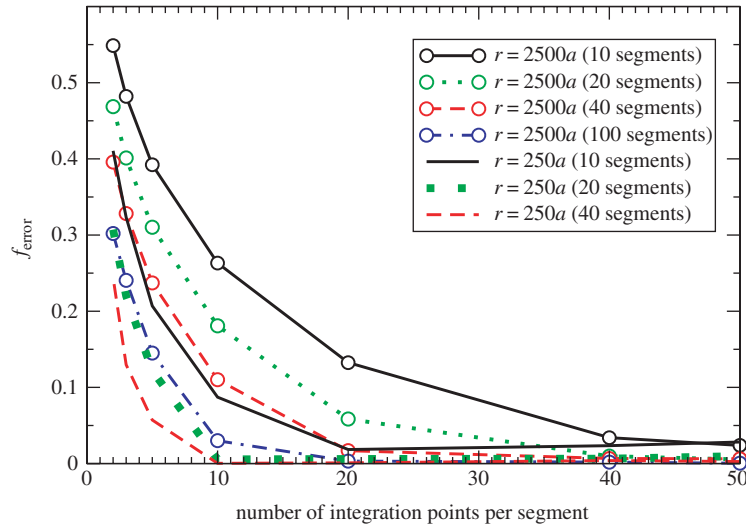


**Figure 6.** Relative error,  $f_{\text{error}} = (1/n) \sum_{i=1}^n [\|f_{\text{analytical},i} - f_{\text{model},i}\| / \|f_{\text{analytical},i}\|]$ , of the nodal force for circular dislocation loops of different sizes using different discretizations.

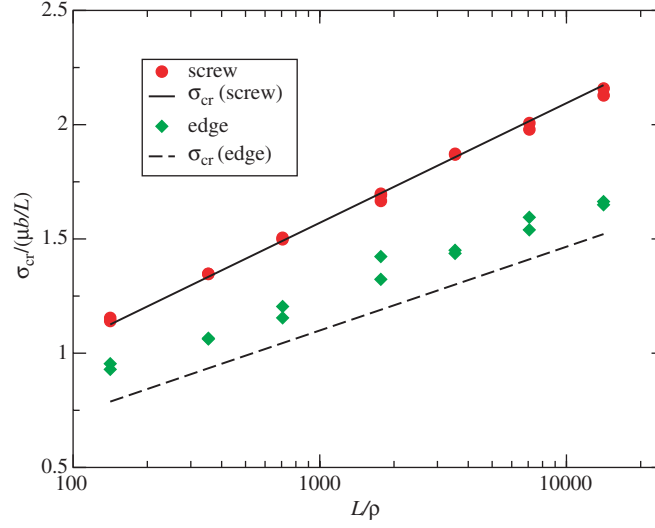


**Figure 7.** Critical activation stress of edge and screw Frank–Read sources of arm length  $L/\rho$ .

simulations with the critical value

$$\sigma_{cr} = \frac{A}{2\pi} \frac{\mu b}{L} \log \frac{L}{\rho} \quad (26)$$

obtained in [25]. Here,  $\mu$  is the shear modulus,  $\nu$  is Poisson's ratio,  $L$  is the arm spacing and  $\rho$  the cut-off length or Brown splitting distance. A value of  $\rho = 2b$  has been chosen. The value of  $A$  is 1 for initially edge oriented sources, and  $1/(1 - \nu)$  for screw oriented sources. This critical stress corresponds to a configuration where the dislocation has bowed out such that ending segments form an angle of  $90^\circ$  to the line defined by the two endpoints of the dislocation. The same condition has been used to determine the critical stresses shown in figure 7. The logarithmic term in equation (26) is reproduced by the dislocation dynamics model. For initially screw oriented sources, very good quantitative agreement between the simulation and the expression (26) is found. The results for the edge dislocation follows a straight line parallel to the analytical expression. The logarithmic dependency is captured. However, a constant offset of about  $0.1\mu b/L$  towards higher critical stresses is observed. The calculations were carried out using between 7 and 50 segments to represent the Frank–Read source.

#### 4.3. Junction formation

A Lomer lock provides an example of junction formation. The geometry is comparable to the one studied in [23, 26].

The initial dislocation geometry is shown in figure 8. The chosen slip systems are  $[01\bar{1}](111)$  and  $[101](\bar{1}\bar{1}1)$  with Burgers vectors of length  $a/\sqrt{2}$ . The intersection line direction of the two glide planes,  $t_{12}$ , is  $[\bar{1}10]$ . The starting geometry of the dislocations are straight lines each having an angle  $\phi$  with  $t_{12}$ . The endpoints of the dislocations are pinned. The midpoints of both initially straight dislocations fall on the intersection line and their mutual distance  $d_{12}$  has been varied between 0 and  $1.4a$ . The initial length  $L_0$  has been chosen to be  $70a$ , but the results change very little when  $L_0$  is increased to  $250a$ . The minimum length of the segments has been set to  $2a$ , the maximum length to  $15a$ . The maximum allowed rotation per time step

$\alpha_{\text{crit}}$  is equal to  $2^\circ$ . Tests with larger values of  $\alpha_{\text{crit}}$  up to  $8^\circ$  have been performed, but with no significant influence on the results. The minimum junction length has been reduced to  $a$  to take into account the lengthscale of interest.

The final lock configuration depends strongly on the initial angle,  $\phi$ . As seen in figure 9, the junctions formed at  $\phi = \pm 45^\circ$  differ from each other. These differences were first studied by Saada [24] using a line tension model. A common way [26, 27] to characterize these differences is to plot the normalized junction length,  $L/L_0$ , versus the initial angle  $\phi$  as in figure 10. The simulation captures the asymmetry between ‘more edge’ (positive  $\phi$ ) and ‘more screw’ (negative  $\phi$ ) type junctions. The edge-type junctions form up to higher angles as they release more elastic energy.

The predictions of  $L/L_0$  versus  $\phi$  from the simulations are plotted in figure 10 along with the predictions obtained from other formulations [26]: line tension models using isotropic and anisotropic line energies (linear isotropic elasticity) [24]; a three-dimensional model using the pure screw/edge type of discretization [2–4]; and a continuous line model including the splitting of dislocations into partials [27] (modelling a Lomer–Cottrell lock instead of a Lomer lock without dissociated dislocations). In [27], two lengths  $l_{\text{jct}(\text{min})}$  and  $l_{\text{jct}(\text{max})}$  have been defined for a junction. Our model agrees closely with the partial dislocation model for the shorter characteristic junction length  $l_{\text{jct}(\text{min})}$  for positive  $\phi$ , whereas for negative  $\phi$ , the anisotropic line tension model is in close agreement for small negative  $\phi$ . For larger negative  $\phi$  the present results fall between the isotropic and anisotropic line tension predictions. Furthermore,

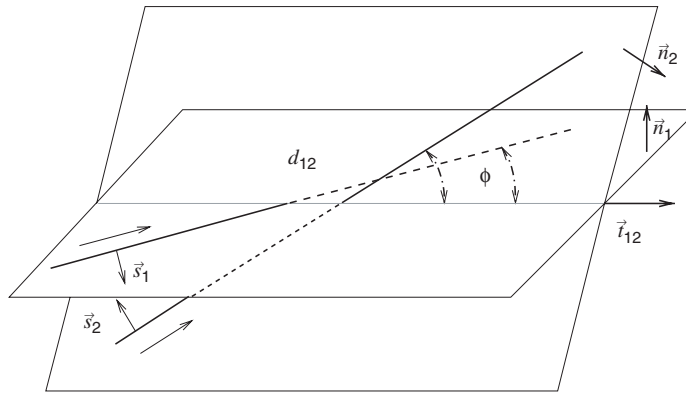


**Figure 8.** The initial configuration. The dislocation line direction is indicated by an arrow. The resolved shear stresses  $f^s$  are in direction  $s_1$  and  $s_2$  for the dislocation in glide planes 1 and 2 respectively. Both dislocations have an angle  $\phi$  with the intersection line of the their glide planes.

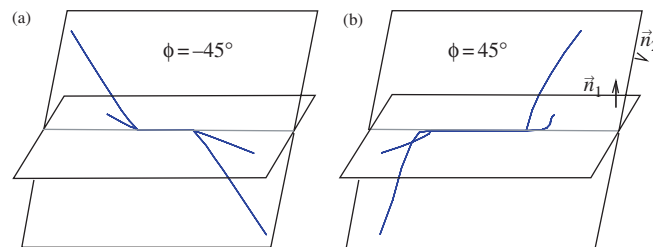


**Figure 9.** The formation of a junction without applied stress and equilibrium configuration: (a) starting from an  $\phi = -45^\circ$  configuration; (b) starting from an  $\phi = 45^\circ$  configuration.

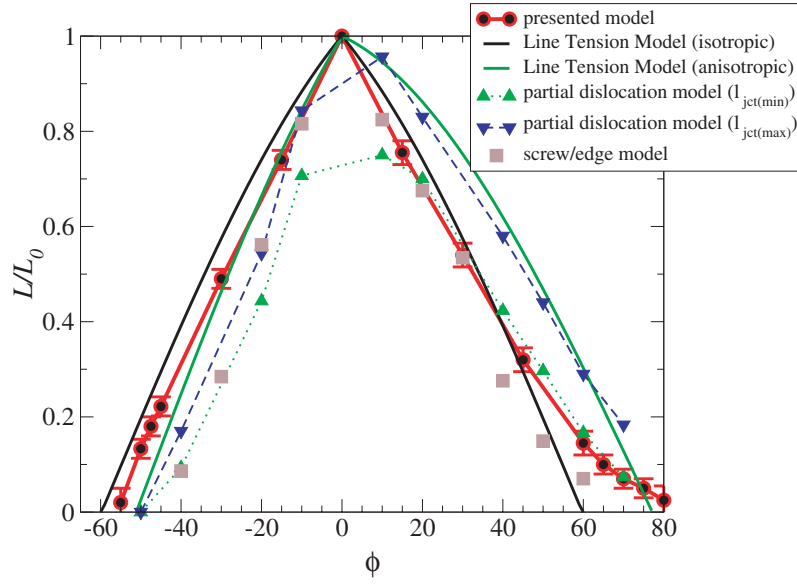


**Figure 10.** The junction length  $L$  versus pinning length  $L_0$  as predicted by various models. The error bars given for the presented model show that the influence of the discretization on the reduced length of the Lomer lock  $L/L_0$  is small.

the present results lead to more stable junctions than the screw/edge model and the partial dislocation model, i.e.  $L/L_0$  is larger and the stability range is wider.

The sensitivity of these results to the initial distance between the dislocations,  $d_{12}$ , is low for small values of  $|\phi|$ . The results are more sensitive to  $d_{12}$  for large negative  $\phi$  close to the point where junction formation is not favourable. For example, the junction for  $\phi = -55^\circ$  is stable for  $d_{12} = 0$  and unstable for  $d_{12} = 2a$ .

#### 4.4. Dissolution of a Lomer lock

The formation of locks is a spontaneous process, but its destruction requires an applied load. First a study of the symmetric junction is done. Its properties are defined in the previous section. This junction is subjected to a ‘symmetric’ external load such that the resolved Peach–Koehler force  $f^s$  on the dislocation in the two glide planes is identical ( $f^s = f_1^s = f_2^s$ ). For values of the resolved Peach–Koehler force less than the value needed for its dissolution, the equilibrium configuration of the junction is shown in figures 11(a)–(c). A snapshot after dissolution of the junction is shown in figure 11(d), where  $f^s = 0.0096\mu b$ . Note that the loading condition is such that the midpoint of the junction remains more or less at the same location.

The behaviour of the junction is quite different for an ‘anti-symmetric’ loading condition for which  $f^s = f_1^s = -f_2^s$ . This junction breaks for  $f^s = 0.013\mu b$ . Under ‘anti-symmetric’ loading conditions the midpoint of the junction moves along the intersection line of both glide planes. The initial intersection point of the two dislocations forming the junction can be quite far away from the point where the junction dissolves. Therefore, it is important in three-dimensional calculations to capture the translation of the junction along the intersection of the corresponding glide planes.

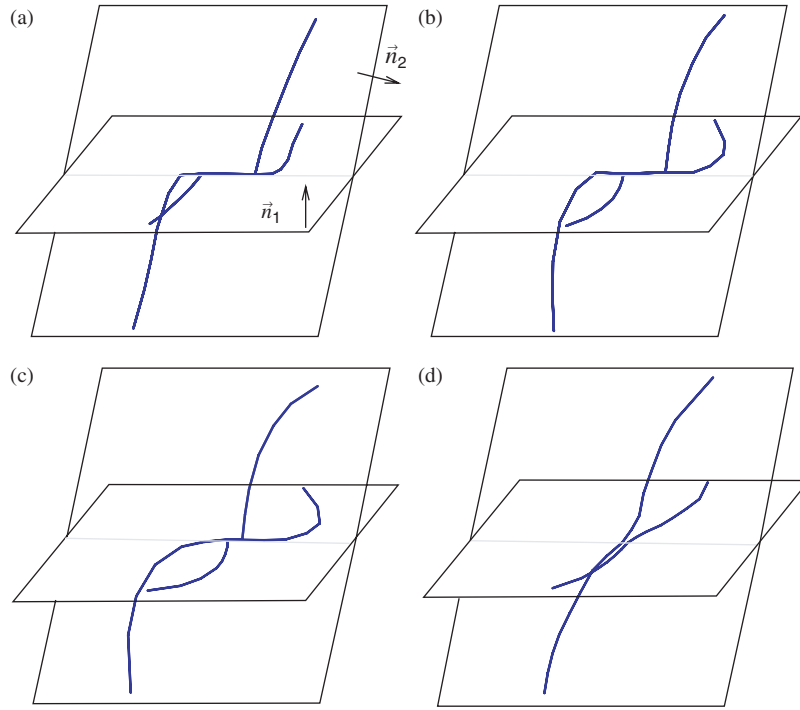


**Figure 11.** A junction of initial geometry  $\phi = 60^\circ$  and  $L_0 = 70a$ : (a) in equilibrium with no applied load; (b) loading under-critical  $f^s = -0.004\mu b$ ; (c) load under-critical  $f^s = -0.008\mu b$ ; (d) snapshot after dissolution applying over-critical load  $f^s = -0.0096\mu b$ .

#### 4.5. Cross-slip

The development of cross-slip is illustrated for two Frank–Read sources, with an initial screw orientation, on parallel glide planes with  $\mathbf{n} = (111)$  at a distance of  $300/\sqrt{3}a$ . The midpoints of the two Frank–Read sources are displaced laterally by  $800a$ . Intermediate slip planes on which cross-slip may take place are inserted with a distance of  $20/\sqrt{3}a$ . A tensile test with imposed displacement in  $y$ -direction is performed. Both Frank–Read sources have the same Burgers vector but opposite initial orientation. Hence, there is an attractive force between the two dislocations. The cross-slip procedure enables a successive approach by multiple cross-slip of both dislocations and finally annihilation of the leading segments takes place. The evolution is shown in figure 12.

### 5. Validation of the boundary-value problem method

The incorporation of the discrete dislocation simulation in a finite volume is demonstrated in simple examples. The first example focuses on the accuracy of the traction cancellation on a surface. In the second example, the force felt by a dislocation from its image field is explored for various configurations. The last example deals with a single Frank–Read source in a thin film, demonstrating the handling of dislocations leaving the volume. The key issue in these examples is how well the correction ( $\hat{\cdot}$ )-fields can be obtained with the finite-element method. It is found in the first two examples that the finite-element solution gives converged image forces even in cases when the traction cancellation at the free surface is not accurate.

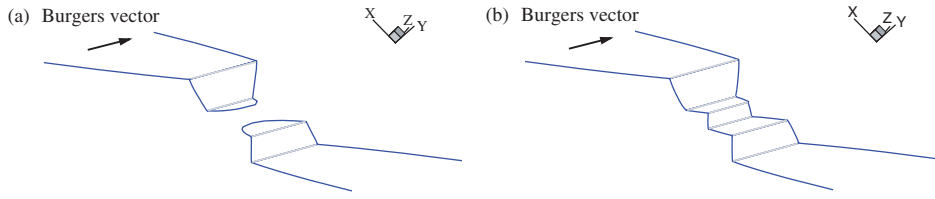


**Figure 12.** Time evolution of two Frank–Read sources in parallel glide planes of same Burgers vector but opposite line directions under applied load in  $y$  direction. (a) The two dislocations have approached. The increasing attractive interaction has triggered cross-slip twice for each dislocation. (b) The two dislocation have meet after further cross-slip events. The dislocation lines of opposite type have annihilated.

### 5.1. Traction cancellation

First, the calculation of image fields using finite elements is illustrated. Calculations with eight-node elements showed that these elements did not capture the variation of the traction  $\tilde{T}_i$  over the surface, especially the components parallel to the surface. Furthermore, the stress fields  $\hat{\sigma}_{ij}$  before averaging at the finite-element nodes were strongly discontinuous, even at relatively large distances from the free surface. Therefore, the calculations are carried out with 20-node elements, using two extrapolation schemes for the  $\hat{\sigma}_{ij}$  stresses, cf section 3.2.2. In the first scheme, the values are extrapolated to all 20 nodes. In the second scheme, the fields based on the eight integration points are extrapolated to the eight corner nodes only, using the shape functions for the eight-node brick. For each surface element the tractions are evaluated at  $3 \times 3$  integration points; for the present problem this was sufficient for convergence.

In both examples, a circular dislocation loop sits inside a cube of side length  $10\,000a$ . In order to check the influence of the orientation of the glide plane with respect to the mesh discretization, two glide plane orientations have been chosen. The surface normals  $\mathbf{n}_s$  of the cube are parallel to (100). Traction-free boundary conditions are used for the whole surface. For all configurations, the norm of the dislocation tractions  $|\tilde{T}_i|$ , and the error in the traction cancellation  $|\tilde{T}_i + \hat{T}_i|/\tilde{T}_{\max}$  for two extrapolation schemes are shown, where  $\tilde{T}_{\max}$  is the maximum value of  $|\tilde{T}_i|$  occurring at the surface.

In the first example, the dislocation lies in the  $x$ – $z$  plane and has a Burgers vector of  $a(100)/\sqrt{2}$ . The centre of the loop is at the centre of the cube. The dislocation is a circle of radius  $4000a$ , leaving a minimum distance to the surface of  $1000a$  at the points of either pure screw or edge orientation. The screw orientations are closest to the  $z = \text{constant}$  surfaces and the edge closest to the  $x = \text{constant}$  surfaces. A  $15^3$  element mesh is used, such that the dislocation glide plane is situated in the middle of a layer of finite elements parallel to the  $x$ – $z$  plane. Figure 13(a) shows the norm of the tractions  $|\tilde{T}_i|$  on the surface and (b) the relative error after the image field correction for the extrapolation schemes using the eight corner nodes only. For both extrapolation schemes, the maximum error is about 20% of  $\tilde{T}_{\max}$  for a dislocation whose closest point is in the second-last layer of elements to the surface. For the eight-node stress extrapolation the error decreases faster with increasing distance from the location of maximal traction. Therefore, the eight-node extrapolation scheme is preferred for this situation. However, this improvement should not be overestimated, since the position of the glide plane with respect to the finite-element mesh is ideal, i.e. it is parallel to the mesh lines.

The influence of the orientation of the dislocation loop with respect to the finite-element mesh is illustrated in the second example. The dislocation is of type  $a/2[1\bar{1}0](111)$ , so that the glide plane (111) is oblique with respect to all cube surfaces. The circular dislocation loop

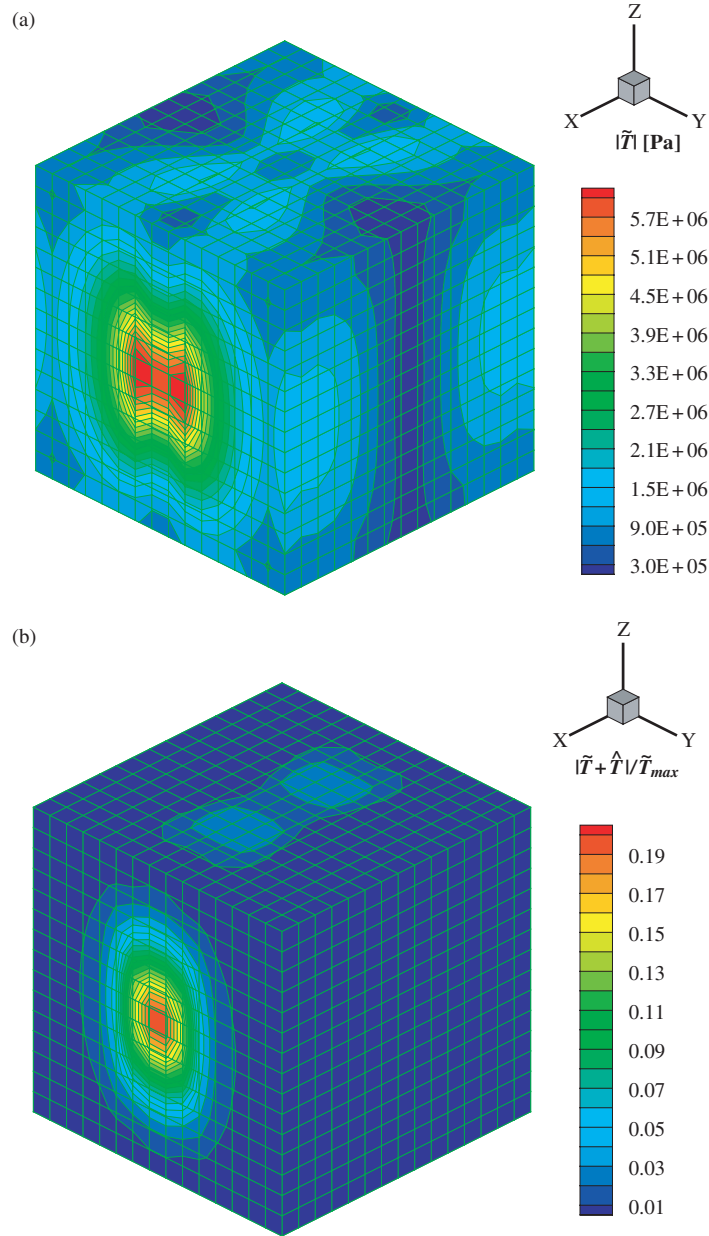


**Figure 13.** Traction cancellation at surface of a cube of side length  $10\,000a$ . Dislocation loop lives in the  $x$ - $z$  plane, having a Burgers vector  $(100)/\sqrt{2}$ : (a) norm of the tractions  $|\tilde{T}|$  over the outside surfaces caused by the dislocation; (b) relative error using eight-node brick based extrapolation.

of radius  $5100a$  is centred at  $(5000a, 5000a, 5000a)$ , and the minimum distance between the dislocation and the surface is  $830a$ . The mesh consists of  $16^3$  20-node elements with side length  $625a$ . In this mesh, the dislocation is going through the finite-element layer next to the last. Figure 14 shows the norm of  $|\tilde{T}_i|$  over the surfaces and the relative errors in the zero-traction condition, as for the previous configuration. The finite-element stress field  $\hat{\sigma}_{ij}$

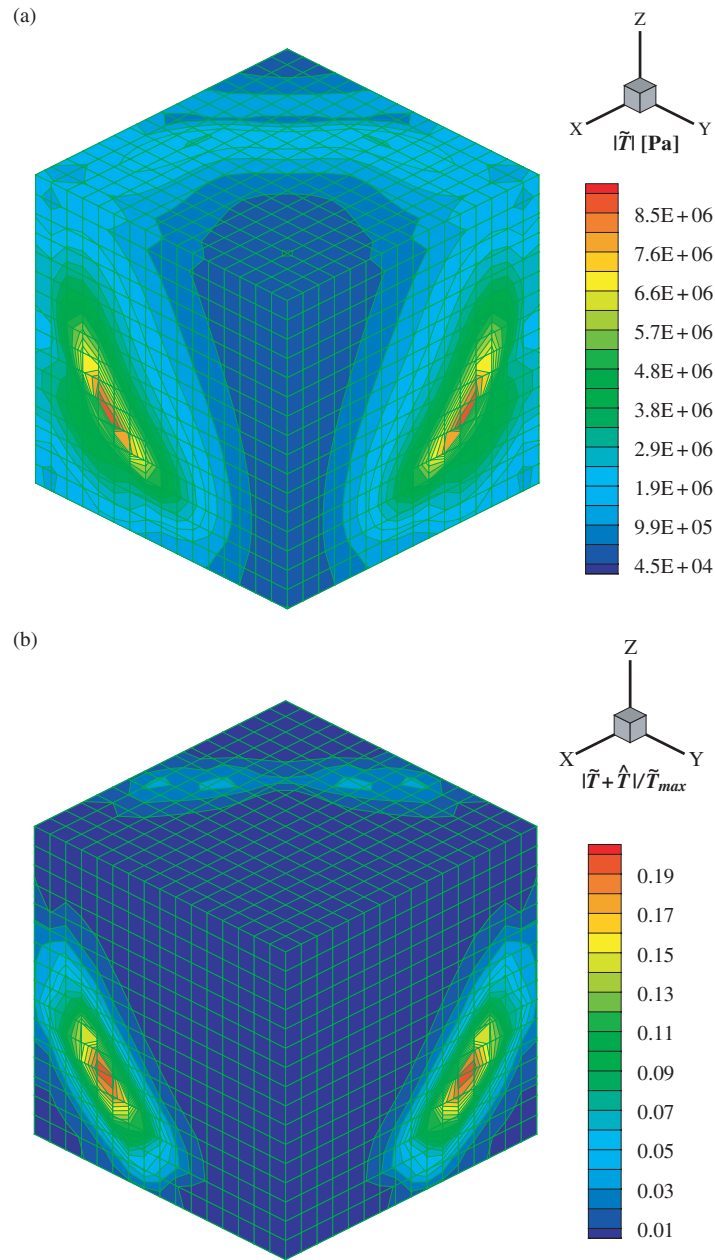


**Figure 14.** Traction cancellation at surface of a cube of side length  $10\,000a$ . The dislocation is of type  $a/2[1\bar{1}0](111)$ : (a) norm of the tractions  $|\tilde{T}_i|$ ; (b) relative error using eight-node extrapolation.

cancels the traction within 20% for the eight-node extrapolation scheme (figure 14(b)) and within 17% for the 20-node extrapolation scheme. The distribution of the error is quite similar for both schemes and therefore only the results for the eight-node extrapolation scheme is shown. The eight-node extrapolation scheme is slightly more accurate around the edges of the volume. Note that the correction is more accurate at the top surface with normal (001), where the nearby part of the dislocation loop is of screw type.



These two examples illustrate the capabilities of the finite-element solution of the  $\hat{\sigma}_{ij}$  fields to cancel the total traction at the surface. It should be noted that the extrapolation scheme is, at the same time, an averaging scheme for the nodal stress values, as each node is shared by several finite elements. Surface nodes are shared by fewer elements, and thus are expected to lead to a larger error for those extrapolated values.

### 5.2. Image forces on dislocations

From the point of view of dislocation evolution, an important issue is how the image fields contribute to the Peach–Koehler force and how this contribution depends on the finite-element discretization. To explore this, we consider the dislocation configuration in figure 14, and use the eight-node extrapolation scheme. Figure 15 gives the absolute values of the dislocation self-forces  $\tilde{F}_{Ai}$  and the image forces  $\hat{F}_{Ai}$  for each of the 100 dislocation nodes. The first node is the one where the dislocation segment is of pure screw type. For all nodes, the two forces point in opposite directions. Finite-element meshes consisting of from  $8^3$  to  $24^3$  20-node elements were used. The nodal forces appear to have converged at a discretization of around  $16^3$  elements, which corresponds to a finite-element side length of  $625a$ . Comparing this length with the minimum distance of  $830a$  between the dislocation and the surface, shows that the image forces are obtained accurately when there is at least one finite element between the surface and the dislocation. When contrasted with the results of the previous section (figure 14), it is seen that the finite element ( $\hat{\cdot}$ )-fields perform much better for image force calculation than for traction cancellation. It is worth noting that the nodal image forces  $\hat{F}_{Ai}$  for the screw parts of the dislocation, which are parallel to the surface in this configuration, have converged even for the coarsest finite-element mesh used. Their magnitude is only 37% of the magnitude of the corresponding nodal self-force  $\tilde{F}_{Ai}$ . The magnitudes of the self-forces and

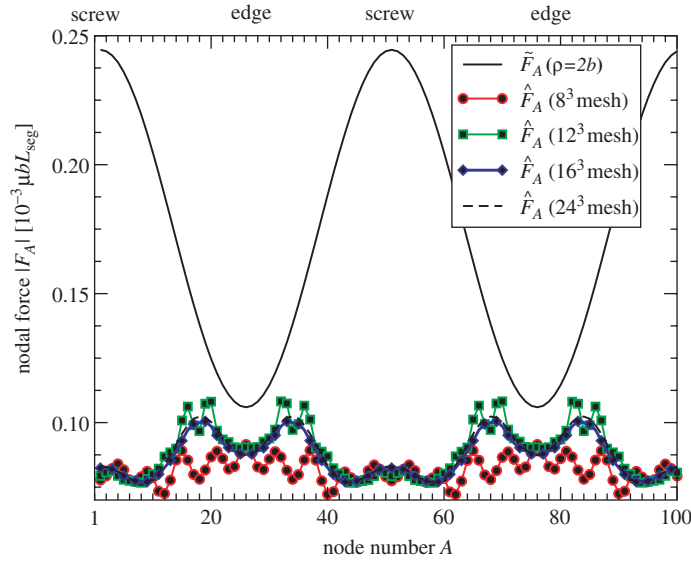


**Figure 15.** Nodal force along dislocation loop: dislocation self-interaction and the finite-element image contribution for different finite-element discretizations. The stress extrapolation is based on the eight-node shape function. The nodal force normalization uses the segment length  $L_{\text{seg}}$  of the loop discretized using 100 nodes.

image forces for the edge part of the dislocation loop are comparable. In this configuration the pure edge-oriented part of the dislocation is relatively far inside the volume compared to the screw oriented part.

The same type of analysis has been carried out for the configuration in figure 13, where both the screw- and edge-oriented parts of the dislocation are at the same distance to the surface. Convergence of the nodal force contribution  $\hat{F}_{Ai}$  in the edge-oriented part of the dislocation is found when there are two to three elements between the dislocation node and the surface. The finite-element size depends, therefore, on the lengthscale of the problem and the needed accuracy for the image forces.

The image field along the two paths marked (1) and (2) in figure 16(a) is considered. Along these paths, the resolved shear stress corresponding to the image stress,  $\hat{\tau} = -n_i \hat{\sigma}_{ij} b_j / b$  is plotted using two finite-element meshes in figure 16(b). Negative values of  $\hat{\tau}$  represent an attractive force to the surface. The values for path (1) are compared to values obtained for an infinite screw dislocation located at a distance of  $1000a$  from the surface of an infinite

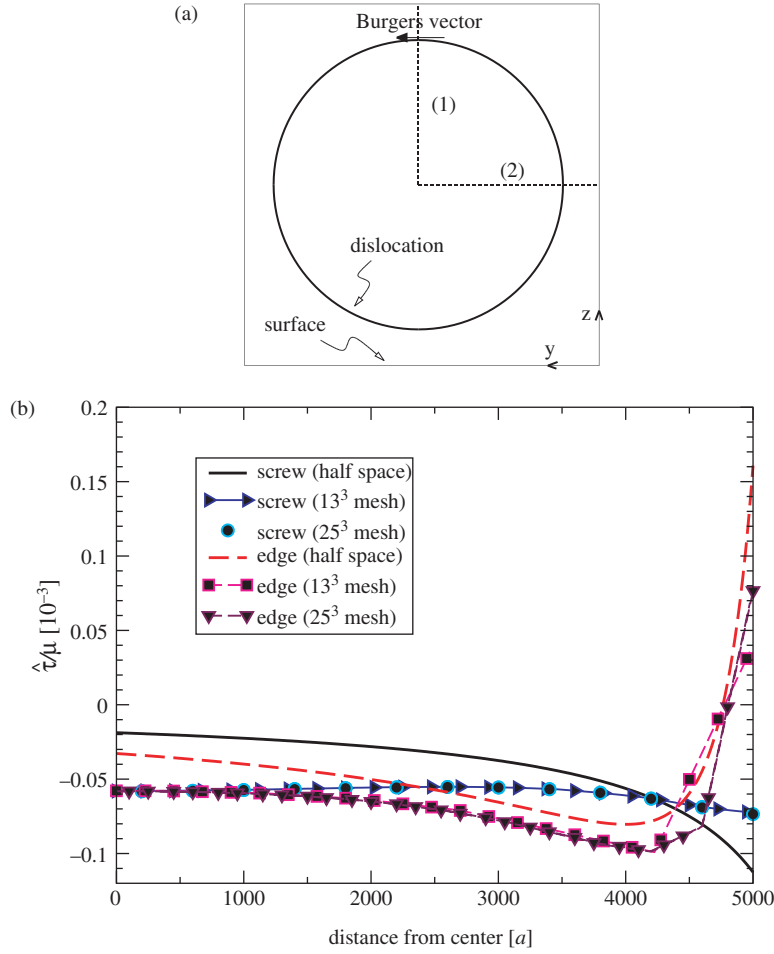


**Figure 16.** (a) Dislocation configuration and paths (1) and (2). The dislocation loop has a radius of  $4000a$ . (b) The image stress  $\hat{\tau} = -n_i \hat{\sigma}_{ij} b_j / b$  in the glide plane with normal  $\mathbf{n}$  is plotted along the path (1) and (2). The dislocation is kept fixed.

half-space [18]. For path (2), the equivalent edge dislocation is chosen for comparison. Both comparisons are expected to be qualitative since the configurations of dislocation in a half-space and a finite cube are quite different. Nevertheless, it can be seen in figure 16(b) that the essentially screw image fields along path (1) and the edge image fields along path (2) are reproduced. Far inside the volume, the finite-element discretization of the cube has no noticeable influence on the image fields. For the screw direction this even holds true along the entire path (1). The edge image fields for the half-space expression shows a sign change for  $\hat{\tau}$  at very small distances from the surface. This sign change is seen in the finite-element solution, but the strong influence of the mesh on  $\hat{\tau}$  close to the surface provides further evidence that at least two elements between the dislocation and the surface are needed.

The previous examples have shared the feature that the entire dislocation is contained in the material volume. The next example addresses a case where dislocations have partly left the volume, leaving a step at the boundary. In section 3.3, virtual dislocations were introduced to improve the accuracy of the nodal forces for such a dislocation geometry. The effect of the finite-element discretization and the number of integration points per element for evaluating the surface tractions  $\tilde{T}_i$  are explored in the following calculations.

The calculations are carried out for a cube of volume  $(10\,000a)^3$ . The glide plane has its normal parallel to the  $y$ -axis of the cube, and contains the centre of the cube. The Burgers vector is in the  $x$ -direction. Traction-free boundary conditions are applied to all surfaces. The quantity compared is the nodal Peach–Koehler force normalized by the total length of the segments shared by the node. This normalization is applied to obtain a quantity that is independent of the discretization of the loop. This dependence holds exactly for a uniform resolved Peach–Koehler force along each segment, as can be seen from the definition of the nodal force components  $F_{Ai}$  in equation (9). Therefore, the normalized nodal force corresponds to a resolved Peach–Koehler force averaged over each segment; its absolute value is denoted by  $f_A$  for node  $A$ . The nodal force  $f_A$  as well as the separate contributions, i.e. the self force  $\hat{f}_A$  and the image force  $\hat{f}_A$  are studied.

In the first example, a circular dislocation loop of radius  $5000a$  is considered. Figure 17(a) shows the location of the dislocation with respect to the volume in a view perpendicular to the glide plane of the dislocation loop. The exit points of the dislocations are at the centre of a surface element. The line directions of the dislocation at the two exit points are parallel to the local normal of surface. The first node shown in figure 17(b) is located in the screw section of the loop, whereas the last node is in a pure edge section. The notation  $(25^3; 5^2, \text{image})$  is used to denote a case with a mesh containing  $25^3$  20-node finite elements; evaluation of the tractions  $\tilde{T}_i$  using  $5^2$  Gauss integration points per surface element and the use of the image construction. Calculations have been performed using  $3^2$ – $20^2$  integration points per surface element for the calculation of the image fields. A selected number of results are shown in figure 17(b), illustrating the effect of mesh size, the number of integration points and the image construction on the nodal forces. The outcome of these calculations is that for the coarser mesh consisting of  $13^3$  cubes,  $10^2$  integration points per surface element are needed to get converged image forces. The verification of convergence is done using a finer mesh consisting of  $25^3$  cubes. Then, convergence has already been found for only  $5^2$  integration points, but it should be noted that the total number of points per face of the cube was roughly the same. Comparing  $f_A$  between both converged results, namely the  $(25^3; 5^2, \text{image})$  and  $(13^3, 10^2, \text{image})$  configurations, it is found that their difference is less than 5% and the maximum difference occurs close to the surface. This suggests that a coarse mesh combined with a large number of integration points per surface element is computationally efficient. These observations hold for both virtual dislocation constructions, i.e. leaving the virtual dislocation as a circular loop (see figure 17(a)(1)) or applying the image construction (see figure 17(a)(2)). Furthermore, figure 17(b) reveals that

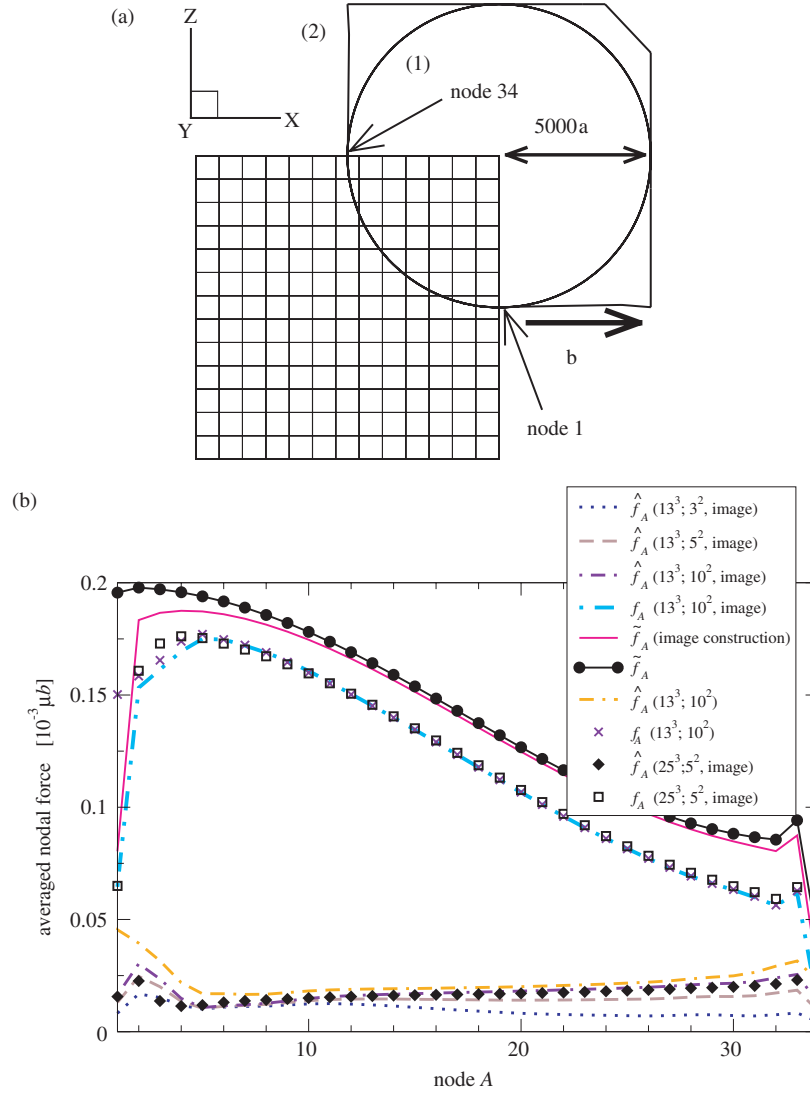


**Figure 17.** Virtual dislocation: (a) location of the dislocation loop in the volume. The dislocation forms a circular loop in (1). The image construction is applied in (2). The in-volume part of the dislocation contains 34 nodes. (b) The different contribution to the averaged nodal force  $f_A$ . The image contribution is denoted  $\hat{f}_A$ . In braces, the finite-element discretization followed by the number of integration point is indicated. The use of the image configuration is marked.

the image construction redistributes the two contributions but leaves the sum  $f_A$  constant. Note that the orientation of the dislocation at the exit points with respect to the surface is an equilibrium configuration. The largest contribution to  $f_A$  is the self-interaction of the dislocation,  $\tilde{f}_A$ .

The automatic re-discretization procedure presented in section 2.2.4 leads to a less perfectly circular loop. In this case, the self-force along the dislocation loop oscillates around the values obtained for an ideal loop, which is at the beginning circular and later on of elliptical shape. These oscillations and deviation from the values of a smooth loop occur during the time

evolution of the discrete structure, but nevertheless on average the forces are correct. This has been tested using different discretization parameters and comparing the evolution of the nodal forces during several consecutive time steps.

The second example involves a dislocation loop of radius  $11\,000a$  placed in the volume as shown in figure 18(a). The path marked (1) in figure 18 shows the circular dislocation loop. Path (2) shows the dislocation configuration after application of the image construction. In this example the line directions of the dislocation at the exit points are inclined with respect to the local surface normals. The exit points are in the centre of a surface element. Starting at

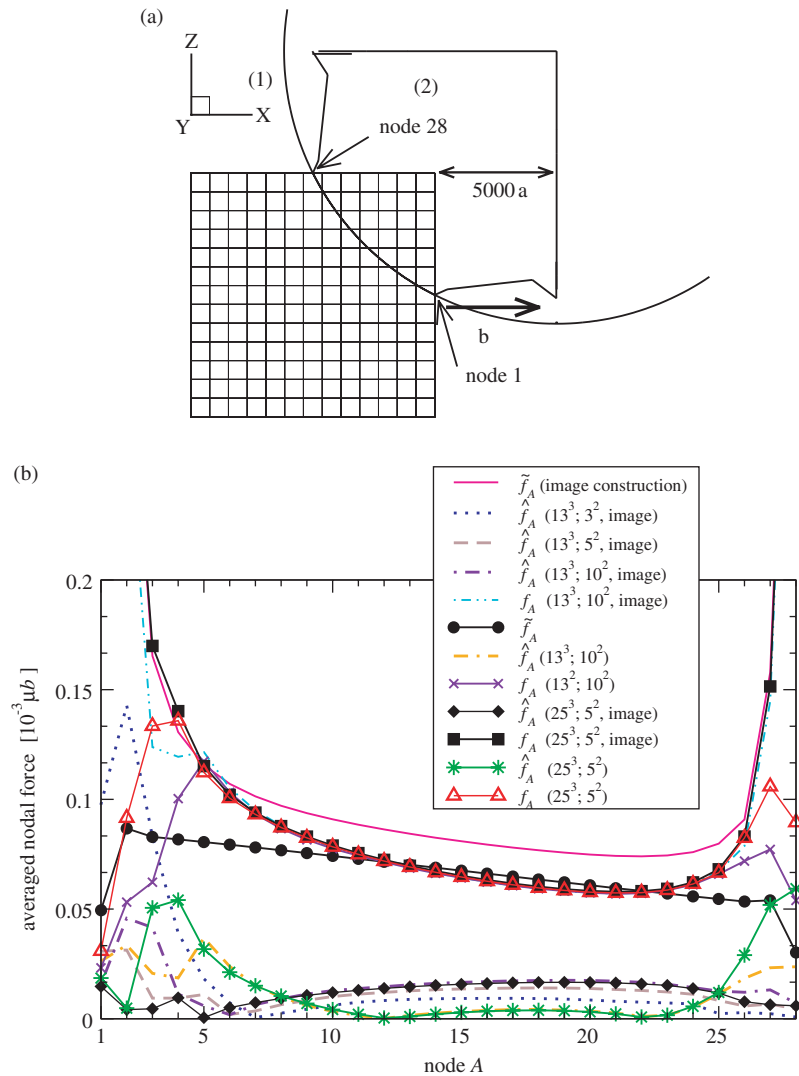


**Figure 18.** Virtual dislocation: (a) location of the dislocation loop in the volume. The dislocation forms a circular loop in (1). The image construction is applied in (2). The in-volume part of the dislocation contains 28 nodes. (b) The different contribution to the averaged nodal force  $f_A$ . The image contribution is denoted  $\tilde{f}_A$ . In braces, the finite-element discretization followed by the number of integration points is indicated. The use of the image configuration is marked.

node 1 (see figure 18), the dislocation orientation changes from ‘near screw’ to ‘near edge’. A mesh consisting of  $13^3$  20-node elements is considered first to emphasize the effect of the image construction. This construction substantially increases the average nodal forces  $f_A$  for the dislocation nodes in the vicinity of the surface, as seen in figure 18(b) by comparing the configurations  $(13^3; 10^2)$  and  $(13^3; 10^2, \text{image})$ . Again,  $10^2$  integration points for each surface element are needed to obtain convergence. As in the previous example, a finer mesh consisting of  $25^3$  20-node finite elements needs only  $5^2$  integration points; the results for this case are used as the reference case in the following discussion. The primary concern is the behaviour of  $f_A$  in the vicinity of the surfaces. Comparing the  $(13^3; 10^2)$  and  $(25^3; 5^2)$  cases with the  $(25^3; 5^2, \text{image})$  reference discretization shows that the steep increase in  $f_A$  close to the surface is not captured by the finite-element solution for the image fields. When the image construction is not applied to the virtual dislocation,  $f_A$  levels off at a value which is related to the finite-element size. In the case  $(13^3; 10^2)$ , the results for the nodes numbered 5–25 coincide with the reference curve. Using a finer mesh  $(25^3; 5^2)$  extends this range by only one node to each side. This confirms two points: (i) the reference curve is reproduced by refining the finite-element mesh, but this refinement is computationally prohibitive compared to the gain in the reproduced range; (ii) the image construction mimics the surface effects on the dislocation itself for dislocation nodes near the surface. Therefore, the image construction allows accuracy to be maintained with coarser finite-element meshes. In addition, the image construction leads to an interesting convergence behaviour of the nodal force contribution from the finite-element solution; close to the surface, both mesh refinement and increasing the number of integration points lead to a lower  $\hat{f}_A$ , whereas the opposite is observed for nodes 6–25, which shows that the virtual dislocation helps to satisfy the imposed traction-free boundary condition.

This example has shown that use of virtual dislocations substantially improves the resolution at nodes close to the surface. This improvement is clearly seen by the convergence of  $f_A$  with increasing mesh refinement, with an increasing number of integration points per surface element and by using the geometrical image construction.

### 5.3. Free-standing thin film

A thin film of dimensions  $10\,000a \times 20\,000a \times 2000a$ , corresponding to  $4.4\,\mu\text{m} \times 8.8\,\mu\text{m} \times 0.88\,\mu\text{m}$  for Al, is analysed which contains a single Frank–Read source of type  $a/2[110](111)$  in pure screw orientation. The source is located at the centre of the film and its arm length is  $0.22\,\mu\text{m}$ . Displacement boundary conditions are applied in  $y$ -direction for the surfaces  $y = 0$  and  $y = 8.8\,\mu\text{m}$ ; all other boundary conditions are zero tractions. A mesh containing  $15 \times 30 \times 10$  20-node elements is used. The minimum length of the dislocation segments has been set to  $50a$ , the maximum length to  $500a$ . The maximum allowed rotation of a segment is  $6^\circ$ . The maximum number of sub-time-steps is 10. For each surface element  $5^2$  integration points are used to evaluate the dislocation traction at the surface. The applied  $y$ -displacements on the boundaries give rise to a Peach–Koehler force in the glide plane on the Frank–Read source which is larger than the force needed to activate the source. Therefore, the source continuously emits dislocation loops to relax the stress in the thin film. Figure 19(a) shows the dislocation structure after 400 time steps at a prescribed displacement of  $u_y = 12a$ . The colours on the mesh give the magnitude of the  $\tilde{u}_y$  displacement. After 2000 simulation steps, the source has emitted a large number of dislocations, several of which have left the film, leaving displacement jumps on the free surfaces, see figure 19(b). These jumps are exaggerated because the deformed mesh is shown using a magnification factor of 50 for the dislocation contribution  $\tilde{u}_i$ .

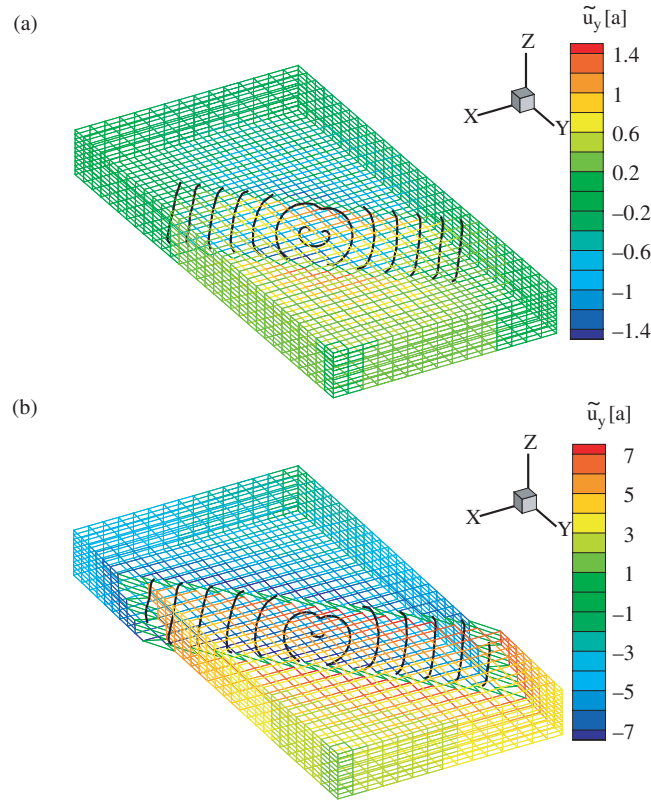


**Figure 19.** A thin film under tension at two stages of uniaxial tension. The colours denote the level of the dislocations  $\tilde{u}_y$  displacements in the tensile direction  $y$ . The deformed mesh is plotted with the dislocation displacements magnified by a factor of 50.

## 6. Conclusion

A three-dimensional nodal dislocation formulation has been presented which builds on an existing nodal model [6] and which incorporates key aspects of dislocation dynamics, namely: continuous evolution of the dislocation structure; junction formation, evolution and dissolution; as well as proper handling of general boundary conditions by use of a finite-element method. The approach has been validated in two contexts; first, for dislocations in an infinite solid and second, for dislocations in a bounded solid.

The tests performed in the context of an infinite volume included calculation of the self-force of a circular loop, the activation stress and size effects of a Frank–Read source, the formation and destruction of a Lomer lock and cross-slip of attracting screw dislocations. These tests serve to validate the dislocation discretization procedures, the Peach–Koehler force calculations and dynamics, as well as the handling of junctions. The tests on formation and dissolution of junctions have shown that the model is able to describe this process in the framework of linear elasticity using non-dissociated dislocations.

In the second context, the treatment of boundary conditions on finite volumes and the resulting calculation of image forces were validated. The tests include dislocation configurations that were entirely inside a finite volume, partially inside a finite volume and

partially out, and continuous straining of a finite slab. Using the finite-element method to obtain accurate image forces is much more of a challenge in three dimensions than in two dimensions. In the three-dimensional formulation, dislocations leaving the volume either partly or entirely must be dealt with explicitly. The finite-element method was shown to give converged image forces for non-intersecting dislocations when there are at least one to two elements between the dislocation and the free surface. Furthermore, the freedom to choose the virtual dislocation configuration can be exploited to give more accurate image force calculations for dislocations intersecting a free surface. This improvement is obtained by implementing a mirror-image construction at the free surface for the intersecting segments.

### Acknowledgments

This research was carried out under project number MS97006B in the framework of the Strategic Research programme of the Netherlands Institute for Metals Research ([www.nimr.nl](http://www.nimr.nl)). A N is pleased to acknowledge support from the Materials Research Science and Engineering Center on *On Micro-and-Nano-Mechanics of Electronic and Structural Materials* at Brown University (NSF Grant DMR-0079964).

### References

- [1] Arzt E 1998 *Acta Mater.* **46** 5611
- [2] Kubin L P, Canova G, Condat M, Devincere E, Pontikis V and Bréchet Y 1992 *Nonlinear Phenomena in Materials Science* vol II, ed G Martin and L P Kubin (Sci-Tech, Vaduz) p 455
- [3] Fivel M C 1997 *PhD Thesis* INP, Grenoble, France
- [4] Verdier M, Fivel M C and Groma I 1998 *Model. Simul. Mater. Sci. Eng.* **6** 755
- [5] Zbib H M, Rhee M and Hirth J P 1998 *Int. J. Mech. Sci.* **40** 113
- [6] Kukta R V 1998 *PhD Thesis* Brown University
- [7] Schwarz K W 1999 *J. Appl. Phys.* **85** 108
- [8] Ghoniem N M and Sun L Z 1999 *Phys. Rev. B* **60** 128
- [9] Ghoniem N M and Huang J 2001 *J. Phys. IV France* **11** pp 5–53
- [10] Fivel M C, Gosling T J and Canova G R 1996 *Model. Simul. Mater. Sci. Eng.* **4** 581
- [11] Van der Giessen E and Needleman A 1995 *Model. Simul. Mater. Sci. Eng.* **3** 689
- [12] Lemarchand C, Chaboche J L, Devincere B and Kubin L P 1999 *J. de Phys. IV* **9** 271
- [13] Yasin H, Zbib H M and Khaleel M A 2001 *Mater. Sci. Eng. A* **309–310** 294
- [14] Johnston W G and Gilman J K 1959 *J. Appl. Phys.* **30** 129
- [15] Greenman W F, Vreelandt T and Wood D S 1967 *J. Appl. Phys.* **38** 3595
- [16] Cleveringa H H M, Van der Giessen E and Needleman A 1967 *Acta Mat.* **45** 3163
- [17] Brown L M 1964 *Phil. Mag.* **10** 441
- [18] Hirth J P and Lothe J 1982 *Theory of Dislocations* 2nd edn (New York: Wiley)
- [19] Devincere B 1996 *Solid State Com.* **93** 875
- [20] Barnett D M 1985 *Phil. Mag.* **A 51** 383
- [21] Cleveringa H H M, Van der Giessen E and Needleman A 2000 *J. Mech. Phys. Solids* **48** 1133
- [22] Nicola L, Van der Giessen E and Needleman A 2001 *Mat. Sci. Eng. A* **309–310** 274
- [23] Bonneville J, Escaig B and Martin J L 1988 *Acta Metall.* **36** 1989
- [24] Saada G 1960 *Acta Metall.* **8** 841
- [25] Foreman A J E 1967 *Phil. Mag.* **15** 1011
- [26] Shin C S, Fivel M C, Rodney D, Phillips R, Shenoy V B and Dupuy L 2001 *J. Phys. IV France* **11** pp 5–19
- [27] Shenoy V B and Kukta R 2000 *Phys. Rev. Lett.* **84** 1491
- [28] Shen Y-L, Suresh S, He M Y, Bagchi A, Kienzle O, Rühle M and Evans A G 1998 *J. Mater. Res.* **13** 1927–37